POLITECNICO DI TORINO

Master's Degree in Aerospace Engineering

Master's Degree Thesis

Preliminary design of a Floating Spacecraft Simulator for a Hardware-In-the-Loop testbed with a matching plane to simulate reduced gravity conditions

Supervisors

Prof. Paolo MAGGIORE

Dr. Giuseppe GOVERNALE

Mr. Armando ATZORI

Candidate

Riccardo COLIA

April 2025

Abstract

Simulating maneuvers in microgravity is challenging due to the unique physical conditions given by the space environment, which are difficult to replicate on Earth. These simulations are vital for developing operational protocols and proximity maneuver algorithms, helping to identify challenges, such as the precise control of the spacecraft during the maneuvers and to optimize algorithms, in terms of reducing time and power, to adjust the maneuver before the integration on the real spacecraft. As space missions become more complex, improving the fidelity and reliability of these simulations is crucial to ensuring mission success. The objective of this thesis is to delve into the most commonly used technologies that can replicate some conditions of a microgravity environment, that are the parabolic flights, the drop towers and the Floating Spacecraft Simulators(FSS) and then to analyze more deeply the FSS coupled with a granite matching plane.

First, the thesis will focus on the design process of the FSS using Systems Engineering (SE) principles and elements identifying system requirements through SE tools such as the functional tree, the N2 matrix and the functions/products matrix. With this structured approach, it is possible, using the Analytic Hierarchy Process(APH) method, to select components that meet specific performance criteria, while also guaranteeing modularity and versatility in experimental configurations. The FSS incorporates AI-driven capabilities to enhance algorithm's training and test of autonomous systems in order to achieve real-time adjusted simulated maneuvers. AI integration is important because the implementation of AI-based techniques is increasingly recognized as a key enabler in space applications in the last years, with numerous studies exploring its potential to enhance spacecraft autonomy and control. Among these, Guidance and Control Neural Networks (G&CNETs) have been proposed as a promising alternative to traditional onboard guidance and control systems, potentially replacing them with simplified neural models. Furthermore, reinforcement learning (RL) is being investigated as a method for empowering adaptive decision-making in unpredictable environments, such as autonomous navigation in space. One particularly relevant application involves the use of these techniques to maneuver spacecraft in non-uniform gravitational and rotational fields, where real-time adaptability is crucial for mission success. The implementation of the AI will be a crucial point for the next FSSs generation and in general for all the space applications involving the use of the GN&C alghoritms.

Then, the granite matching plane is taken into consideration mostly from a logistical perspective, with a preliminary planning of its installation inside a

dedicated laboratory, due to the importance of a properly functioning testbed for the success of the project, ensuring the precision required for these applications. Trade-offs are assessed to determine the optimal installation position, considering the laboratory structural constraints and already present infrastructures layout. Subsequently, a preliminary installation plan is also presented from the unloading of the granite plane from its transportation vehicle to its desired positioning inside the laboratory, including the selection of the appropriate transportation vehicle for a massive-weight granite plane and the determination of the installation process within the laboratory by demolishing a drywall partition in order to facilitate the granite plane's entry and placement in the laboratory.

Acknowledgements

Heartfelt thanks to Giuseppe and Armando for all the support and help you have given me, enriching this final stage of my academic journey. A big thank you also to all the ASTRADORS for the precious moments we shared together.

I would also like to thank professor Paolo Maggiore for taking on the responsibility of this thesis.

Table of Contents

List of Tables

List of Figures

VIII

Acronyms

AI

    Artificial Intelligence

FSS

    Floating Spacecraft Simulator

MBSE

    Model Based System Engineering

ISS

    International Space Station

NASA

    National Aeronautics and Space Administration

JPL

    Jet Propulsion Laboratory

FCT

    Formation Control Testbed

PACMAN

    Position and Attitude Control with Magnetic Navigation

SSDT

    Small Satellite Dynamics Testbed

DOF

    Degree Of Freedom

SPART

Spacecraft Robotics Toolkit

GNC

Guidance Navigation and Control

OBC

On-Board Computer

IMU

Inertial Measurement Unit

TCS

Thermal Control Unit

EPS

Electrical Power System

HIL

Hardware-In-the-Loop

HPA

High Pressure Air

MSA

Motion Support Actuator

RL

Reinforcement Learning

NN

Neural Network

CNN

Convolutional Neural Network

DL

Deep Learning

AHP

Analytically Hierarchical Process

ADCS

Attitude Determination & Control System

Chapter 1

Introduction

Testing GN&C algorithms for maneuvers such as docking alghorithms in a controlled laboratory environment is essential, as it drastically reduces costs and risks compared to other testing options such as parabolic flights and drop towers. Moreover, optimizing these algorithms allows for more accurate results, ensuring their reliability during integration into the spacecraft.

This thesis focuses on the design of a Floating Spacecraft Simulator (FSS), with a strong emphasis on integrating an advanced artificial intelligence (AI) processing unit to enable simulate autonomous maneuvers such as obstacle avoidance and docking, crucial for realistic space mission training. By employing iterative learning, the AI enhances the FSS's capability to execute complex maneuvers, analyzing and adapting to trajectory and orientation adjustments to ensure safe and effective automation of these operations.

The design of the FSS follows a Systems Engineering (SE) approach, with the main focus on the definition of the system architecture using SE tools such as the N2 matrix and the functions/products matrix to define the subsystems, their key components and their interaction with other subsystems. This methodology ensure a structured preliminary design process. In addition, using the AHP method it is possible to select the best components that meet the system requirements in Section 3.4. The FSS utilizes advanced air-bearing technology to achieve three degrees of freedom, two translational and one rotational, a typical configuration of the dynamic simulators that operate in laboratory environment for the GN&C algorithms testing.

This thesis is structured as follows: in Chapter 2 a general overview of the gravity reduced existing technologies is presented, highlighting their distinctive features and applications. Chapter 3 presents the design of the FSS, beginning with a Systems Engineering (SE) approach [7], which outlines the process of defining the system's requirements and functionality, shaping a preliminary design of the FSS. This method ensures a structured and efficient design process, emphasizing the

critical integration of AI-ready components that enable future implementation of machine learning algorithms. It is important to note that this work focuses solely on the selection of components that allow AI integration, without addressing the actual implementation of machine learning algorithms.

In addition to the FSS design, in chapter 4 the thesis addresses the logistical challenges involved in transporting and precisely installing a granite matching plane, which will serve as the gravity-reduced platform necessary for Hardware-In-the-Loop, HIL, testing. The surface of the granite plane must have a high level of flatness to ensure accurate dynamic simulations. The planning and execution of its installation within the laboratory at Politecnico di Torino involve overcoming significant logistical challenges, including transportation and setup.

Chapter 2

Reduced gravity simulators

Microgravity is a critical condition for the success of space missions, as the differences from the Earth's environment can lead to unexpected behavior in materials and devices, compromising mission outcomes. To address these challenges, it is essential to test all devices and components under conditions that closely replicate microgravity.

Simulating microgravity on Earth is a significant but necessary task, as direct testing in space would be excessively costly, risky and logistically complex. These Earth-based simulations are crucial for the preliminary testing, development and refinement of technologies destined for use in orbit.

In addition to testing hardware, simulating microgravity also enables the validation of algorithms used in on-board systems, such as those for proximity maneuvers and docking operations [8]. Over the years, several methods have been developed to replicate microgravity-like conditions on Earth, including parabolic flights, drop towers and floating simulators paired with low-friction planes.

2.1 Parabolic flight

Parabolic flight is a widely used technique to create short-duration microgravity conditions for scientific experiments, astronaut training and testing of space equipment. This methodology is based on the concept of parabolic motion, a curvilinear trajectory in which an object follows a parabolic path under the influence of gravity. Parabolic flight, often carried out using specially equipped aircraft, simulates microgravity conditions through a series of specific maneuvers designed to mimic free fall.

The concept of parabolic flight relies on the laws of classical physics, particularly Newtonian mechanics that govern the trajectory of a body in free fall. During a parabolic flight the aircraft performs a series of maneuvers called parabolic arcs,

that can be divided into three main phases: the ascent phase, the parabolic phase and the descent phase, as we can see in Figure 2.1.

The initial phase begins at approximately 6,000 meters, with the aircraft traveling at a speed of 810 km/h. From here, the plane enters a steep climb, around 45 degrees, where it accelerates rapidly, generating a sensation of increased gravity, also known as **hypergravity**, typically around 1.5 to 1.8 g. This rapid ascent lasts about 20 seconds, during which the aircraft reaches a peak altitude of 7,500 meters while traveling at 650 km/h [9].

At this point, the engines are throttled back, and the aircraft enters a ballistic trajectory. For the next 10 seconds, the aircraft follows this trajectory, reaching a peak altitude of 8,500 meters. During this phase, both the aircraft and its occupants experience microgravity, which creates the sensation of weightlessness. In this phase, which lasts for **about 20 seconds**, the aircraft, along with everything inside, is in free fall under the influence of gravity alone. During this phase the average value of the residual gravity acceleration during the zero-g parabola is around 10^{-2} - 10^{-3} g [8]. Finally, the aircraft performs a recovery maneuver to reduce its descent and return to normal flight conditions, experiencing another brief period of hypergravity as it levels out.
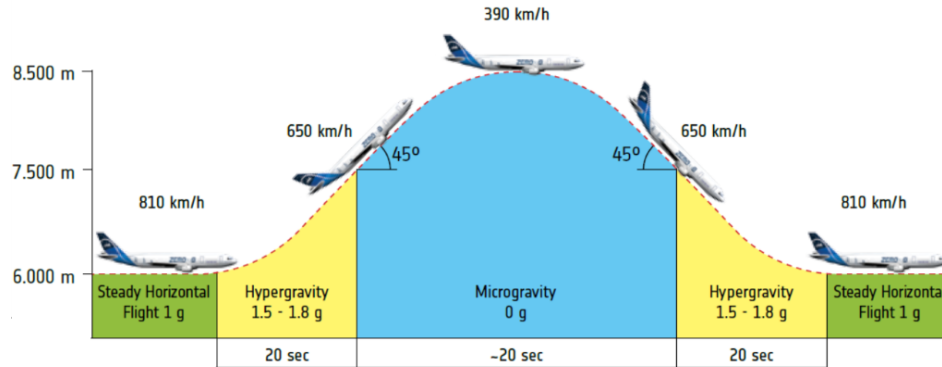
Figure 2.1: The parabolic flight manoeuvre of the Airbus A300 (Credit ESA) [9]

This cycle is repeated several times during the flight, typically up to 30 or more arcs in a single session, allowing for several cumulative minutes of weightless conditions. The advantage of parabolic flights lies in their ability to provide a repeatable and controlled microgravity environment for researchers and astronauts. In the context of space missions, parabolic flights are also used to simulate atmospheric reentry conditions. This simulation is crucial for testing life support systems, reentry mechanisms and other critical technologies that must perform flawlessly during the reentry of a spacecraft to Earth. Through these simulations, researchers

can identify and resolve potential problems before they become hazardous during a real mission. For example, they test how materials and components withstand the stresses of reentry and high-speed flight dynamics.

One example of the use of Parabolic Flight for the test and validation of an aerospace application is the PACMAN, Position and Attitude Control with MAgnetic Navigation, project [10]. The PACMAN experiment aimed to validate a docking system for small satellites that utilizes magnetic actuators in a microgravity environment. This system allows for the control of relative attitude and position between two satellite units using magnetic solenoids and localization sensors, eliminating the need for traditional thrusters and offering advantages in terms of reduced weight and complexity. This is accomplished by launching a miniature spacecraft mock-up, CUBE, and a Free-Floating Target, FFT, that generates a static magnetic field towards each other; a set of actively-controlled magnetic coils aboard the CUBE, assisted by dedicated localization sensors, are used to control its attitude and relative position assuring the accomplishment of the soft docking maneuver. In Figure 2.2 is it possible to see a schematization of the project PACMAN. To test the system, parabolic flights, such as those performed with the Airbus A310 Zero-G, provide short microgravity intervals, around 22 seconds, alternated with hypergravity phases up to 2g. These conditions enable the collection of valuable performance data in realistic environments, helping to demonstrate the effectiveness of the system, study its behavior under microgravity and validate theoretical models with experimental results.
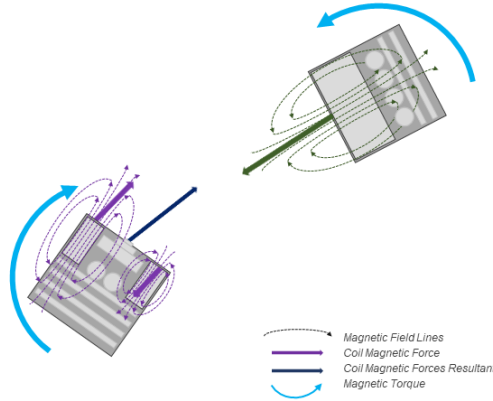
Figure 2.2: PACMAN project schematization [10]

The parabolic flight was chosen as the testing platform for the PACMAN experiment because it provides a controlled microgravity environment crucial for validating technologies intended for space applications. Microgravity overcomes

the limitations of ground-based tests, where gravity and other interfering factors can significantly affect the magnetic interactions studied.

In a ground-based setting, the gravitational force is orders of magnitude stronger than the weak magnetic forces central to the PACMAN experiment, making accurate and reliable measurements nearly impossible. Additionally, the magnetic forces between electromagnets decrease drastically with distance, following the $\frac{1}{r^3}$ relationship. This rapid decay means that when electromagnets are farther apart, their attractive forces become negligible and are easily overpowered by friction or other disturbances. Ground-based experiments are further hindered by friction between contact surfaces, especially at larger distances, which can skew results and render them unrepresentative of the dynamics in space.

The parabolic flight provides an ideal environment to address these challenges. It creates microgravity conditions 10^{-2}–10^{-3} g , which replicate the orbital environment, allowing for a much more accurate analysis of magnetic interactions and the associated dynamics. Unlike ground-based setups, which are constrained by supports, cables and limited to two-dimensional movements, the parabolic flight offers a free, three-dimensional testing space. This setup ensures that the experiment is not affected by structural constraints or external interferences, leading to more realistic results. Furthermore, ground-based equipment connections can alter the physical characteristics of the system, such as its mass distribution and center of gravity, whereas these factors are not an issue during parabolic flight.

Compared to other methods, parabolic flights offer several advantages. While drop towers provide even higher microgravity levels, the limited duration and frequency of the tests make them less suitable for iterative experiments. Parabolic flights, on the other hand, allow for longer periods of microgravity, about 20 seconds per parabola, repeated multiple times within a single session. This makes it possible to gather sufficient data for statistically valid conclusions, even in cases of experimental anomalies. The ability to modify parameters between test runs, interact with the equipment, and adapt to unforeseen issues ensures that results can be optimized in real-time, maximizing the data collected.

The flexibility to conduct multiple tests over consecutive days and analyze the outcomes between flights further enhances its value. The larger test volume within the aircraft also supports more complex setups and interactions compared to drop towers

Overall, the parabolic flight provided an optimal balance of realistic microgravity conditions, repeatability, and operational flexibility, making it an essential step in increasing the Technology Readiness Level, (TRL), of the PACMAN system. This environment enabled precise validation of the magnetic interactions and dynamics critical for future space applications, such as on-orbit servicing and deorbiting operations.

But this is just one example of the possible applications in the aerospace field,

many of which were initiated through the ESA Fly Your Thesis! program [11]. Among these, alongside PACMAN, is the SatLeash experiment [12]. This project focuses on studying the dynamics and control of tethered tugs, an innovative approach to space transportation with applications such as active debris removal, satellite de-orbiting and asteroid retrieval.

The experiment uses a reduced-scale testbed to simulate the interaction between a passive target and an active chaser connected by a flexible tether. To ensure the validity of the developed control laws and numerical models, SatLeash leverages parabolic flights to recreate microgravity conditions, allowing precise investigation of the tether's behavior during tensioning and release phases. These tests are crucial for mitigating critical instabilities, such as whiplashes and bounce-back effects, which can pose significant risks during tethered operations in space.
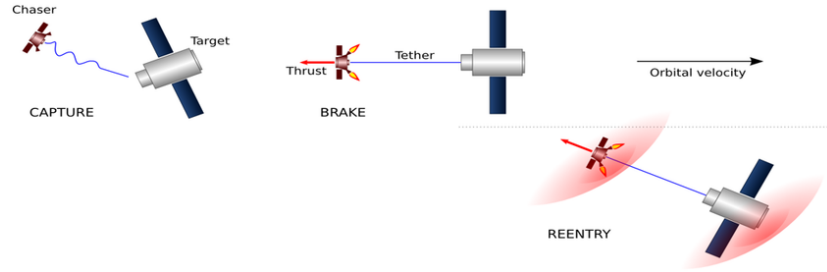
Figure 2.3: Tethered-Tug Concept [12]

2.2   Fall Towers

Fall towers, also known as drop towers, are vertical structures designed to simulate microgravity by allowing objects to fall freely. When an object is released from the top, it enters free fall and experiences apparent microgravity condition. The duration of the fall, and thus the microgravity, **depends on the tower's height**, with taller structures offering longer periods, ranging from fractions of a second to several seconds. This method achieves a residual gravity acceleration around 10^{-3} to 10^{-6} g [8]. It is highly beneficial for experiments that require a short but precise microgravity environment.

Fall towers are essential for testing space robotics by simulating microgravity conditions. They help engineers evaluate robots' functionality, control, and navigation systems for tasks such as docking, assembly, and repairs. Additionally, fall towers are used to test microsatellites and space drones, ensuring the precision of propulsion, stability, and task performance in microgravity.

One of the main advantages of fall towers is their relative cost-effectiveness.
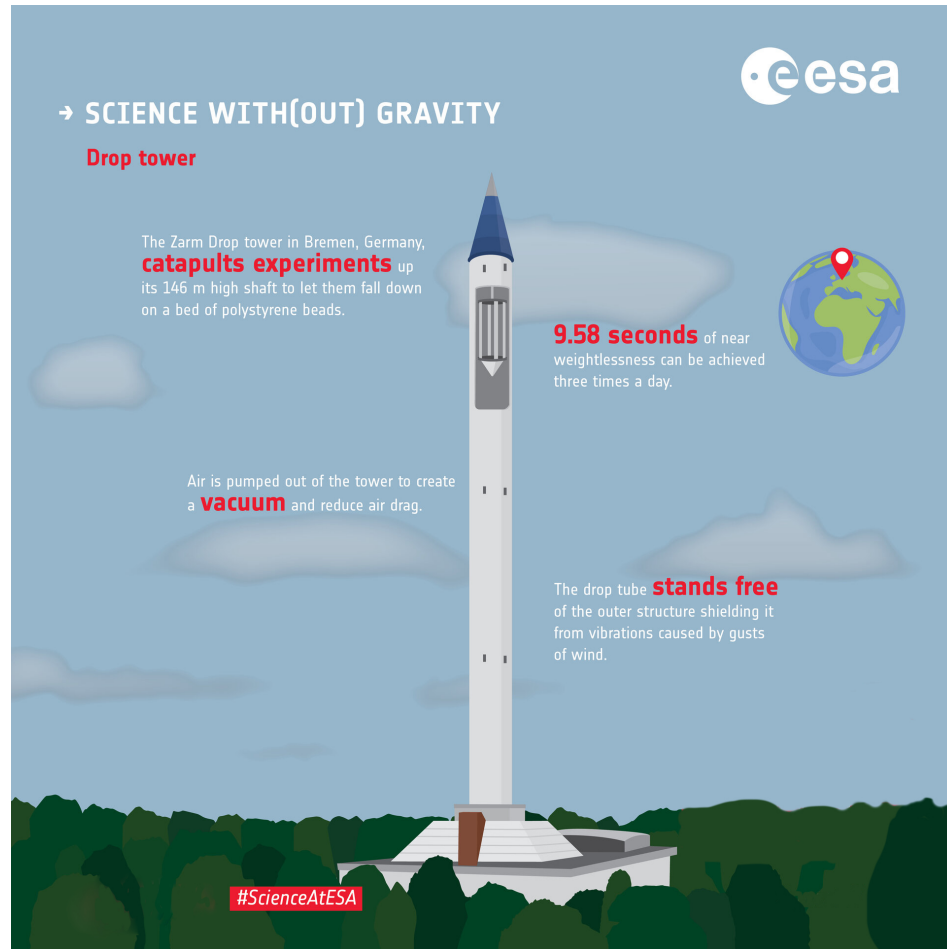
Figure 2.4: Credit:European Space Agency (ESA), Mechanism of Fall Towers [13]

Compared to parabolic flights and space launches, they offer a more economical solution for simulating microgravity, making them accessible to a broader range of researchers. Additionally, fall towers provide a controlled environment for experiments. Temperature, humidity and other factors can be precisely managed, ensuring that the results are not influenced by external variables. This precise control enhances the reliability and reproducibility of the data collected.

However, there are some limitations to fall towers. The primary drawback is the short duration of microgravity, which may not be sufficient for certain complex experiments, such as those involving biological growth or fluid dynamics that require longer periods of weightlessness. In these cases, other methods, such as parabolic flights or orbital experiments, may be necessary.

Furthermore, the size of the objects that can be tested is limited by the tower's

dimensions, restricting more complex or larger equipment from being tested. This constraint may be a significant challenge for some projects.

The capsule's release mechanism is a crucial component of the fall tower. In Figure 2.5, we see the release mechanism. Various systems, such as electromagnetic, pneumatic shearing bolts and cutting wire methods, ensure a smooth, vibration-free release.[14]

During free fall, the capsule experiences air resistance, or drag, which reduces the quality of microgravity achieved. Various methods are used to mitigate or eliminate this effect. One common approach is removing air inside the tower to create a vacuum or near-vacuum condition, which minimizes drag to the greatest extent possible. However, evacuating the tower requires a significant amount of power and time, reducing the number of experiments that can be conducted and increasing operational costs per experiment.

Another strategy involves designing the capsule to be streamlined, which is particularly effective in towers with shorter drop times. Nevertheless, for towers with longer drops, streamlining by itself does not sufficiently reduce drag.

A more advanced solution is the capsule-in-capsule methodology. Here, the main experimental capsule is enclosed within a larger outer capsule that acts as a drag shield. If the outer capsule is evacuated, the inner capsule experiences free fall in a near-perfect vacuum, eliminating drag. Even when the outer capsule is not vacuumed, the drag acting on the inner capsule is significantly reduced due to the minimal relative velocity between the two capsules, ensuring good quality microgravity. This concept is also applied in drop balloon platforms like Ballon Operated Vehichle(BOV) [15], which extend the microgravity period by using gas jets to prevent the inner capsule from impacting the drag shield. However, managing drag with such systems becomes increasingly complex in changing atmospheric conditions, making it challenging to achieve high-quality reduced gravity.

The release mechanism is critical to ensuring a smooth and instantaneous release of the capsule without tilting, swaying, or inducing vibrations, as these factors negatively affect microgravity quality.

Electromagnetic release systems rely on a powerful electromagnet to hold the capsule at the top of the tower, releasing it when the magnet is demagnetized. While this method is effective, it requires a continuous power supply and can experience delays during the demagnetization process, which may cause the capsule to tilt. Moreover, power failures pose a significant safety concern, as they could trigger an unintended release.

On the other hand, the pneumatic shearing bolt mechanism works by shearing the threaded bolt that holds the capsule in place. Nonetheless, this system can result in rough releases due to friction between the bolt and its attachment. This friction often generates low-frequency vibrations that can disturb the quality of the microgravity environment.

9
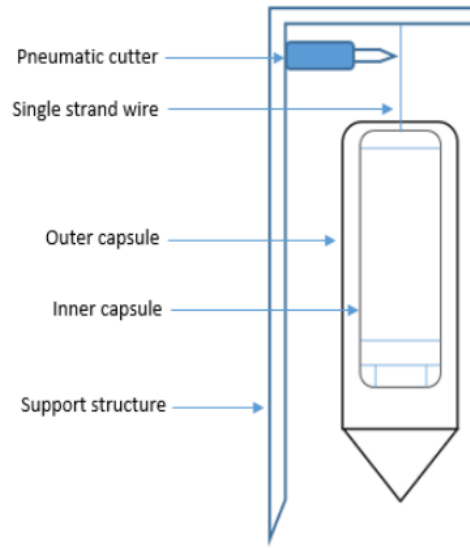
Figure 2.5: Pneumatic release mechanism of the capsule[14]

Lastly, while fall towers simulate microgravity effectively, they cannot fully replicate the conditions of space, such as the vacuum environment, cosmic radiation and long-duration exposure to microgravity. This limitation affects the comprehensiveness of the tests conducted within drop towers, necessitating complementary testing methods to simulate a more complete space environment.

At the moment, fall towers are heavily used for fluid studies, particularly on combustion [16] but also for researches in the field of physics, like the one that tests the Weak Equivalence Principle of the General Relativity [17], but since these fields deviate from the topic of this thesis we are not going to examine these applications related to the chemical and physical processes.

2.3 Floating Spacecraft Simulators with Matching Plane

FSS have been instrumental in spacecraft development for over 30 years. Their evolution has paralleled that of actual spacecrafts, constantly integrating advanced technologies and innovative methodologies. This chapter provides an overview of the state of art and the recent advancements in the field of FSS.

Floating simulators represent a significant advancement in the field of spacecraft dynamics testing. These sophisticated systems utilize planar air-bearing technology to create a frictionless environment, enabling the simulation of three degrees of freedom (3-DOF) for various applications[18].

The core technology behind floating simulators is the use of air bearings, which allow for low-friction motion on a horizontal surface. By generating a thin layer of pressurized air these bearings enable a spacecraft model to float above the surface, significantly reducing the effects of gravity and friction. Recent advancements in this technology, thanks to more accurate technologies and algorithms, have led to improved precision and stability, making it possible to replicate the dynamics of actual spacecraft in a controlled laboratory environment. Additionally, controlled environmental conditions are necessary to replicate space-like conditions such as consistent temperature, humidity, and pressure levels, ensuring that all aspects of the spacecraft's environment are as close to reality as possible

Physical characteristics such as mass and inertia play a crucial role in accurately simulating spacecraft behavior. Adjusting the mass distribution and inertia properties of the simulator to match those of the actual spacecraft or its components is essential for realistic movement and control. The center of gravity of the simulator must also correspond precisely to that of the actual spacecraft to ensure that the dynamics, especially in response to applied forces and torques, mimic real-world conditions. The simulator must be capable of mimicking the spacecraft's movements, from gentle rotations to rapid maneuvers, to provide an accurate testing environment. Ensuring that forces and torques applied to the simulator during tests are representative of those experienced in space is also critical. These forces could result from thrusters, gravitational influences, or other propulsion systems that need to be precisely replicated.

Operational elements such as control systems and onboard algorithms must be mirrored in the simulator. This includes implementing control algorithms and systems that are similar to those used in the actual spacecraft, including feedback mechanisms that adjust the spacecraft's movements in real time. Sensor and actuator matching is also vital; using sensors and actuators in the simulator that are equivalent to those on the spacecraft ensures similar performance characteristics, which is crucial for testing navigation, docking, and other complex maneuvers.

NASA's Jet Propulsion Laboratory (JPL) continues to lead in FSS technology. Among their notable testbeds is the Formation Control Testbed (FCT)[18] , designed for formation maneuvering. This six-degree-of-freedom (DoF) flat testbed employs flat air bearings for horizontal plane DoFs and a spherical air bearing for rotational DoFs. The FCT is approximately 1.27m wide and weighs around 100kg.

Another significant testbed at JPL is the Small Satellite Dynamics Testbed (SSDT). This testbed, smaller than the FCT, features three DoF and uses eight compressed air thrusters and planar air bearings, both operating at 6.2 bar. Each thruster provides roughly 0.5N of thrust, creating a dynamic and versatile testing

environment. The SSDT weighs around 30kg and measures approximately 0.5m in width.

A recent research [19] introduced a compact planar FSS measuring 30cm x 30cm and weighing about 15kg. This simulator, equipped with eight thrusters generating between 0.3N and 0.4N of thrust, utilizes two Arduinos as the on-board computer, showcasing an innovative approach to FSS design.

Polish researchers have developed a new planar microgravity simulator featuring a base and a manipulator arm with two joints. This simulator, supported by air bearings, offers planar translation, rotation around the vertical axis, and one DoF per joint, amounting to a total of five DoF. The base weighs approximately 13kg, and combined with the arm, the total weight is nearly 19kg.

At the University of Rome La Sapienza, researchers have constructed the PINOCCHIO FSS planar testbed [20] [21]. This setup simulates a satellite's pursuit of a target in space, with the chaser vehicle weighing 8.7kg and measuring 20cm x 20cm x 45cm. The vehicle features separate thruster sets for attitude and location control, including four thrusters for translation and a parallel configuration for rotation, totaling twelve thrusters. The target vehicle uses computer fans for propulsion.

A notable recent development is the open-source SPAcecraft Robotics Toolkit (SPART) [22] by the Spacecraft Robotics Laboratory at the Naval Postgraduate School. SPART is a versatile software toolkit that provides six-degree-of-freedom kinematic and dynamic simulations for spacecraft with robotic arms. It can simulate floating or flying bases and handle external forces, making it ideal for both operational and joint space modeling.The Spacecraft Robotics Toolkit (SPART) is a significant engineering advancement in the field of space robotics, addressing the complex challenges of designing and controlling robotic manipulators mounted on spacecraft. Unlike terrestrial robots, space-based manipulators must account for the dynamic interactions between the arm and the free-floating base, complicating their modeling and control. SPART effectively handles these challenges with a modular and efficient approach, enabling simulation, analysis, and control of such systems.

Practically, SPART is an open-source toolkit developed in MATLAB/Simulink. It simulates both kinematics (coordinate transformations, velocities, Jacobians) and dynamics (inertia and convective matrices) of spacecraft manipulator systems. It employs recursive $O(n)$ algorithms, leveraging the Decoupled Natural Orthogonal Complement (DNOC) matrix to solve forward and inverse dynamics problems efficiently. This makes it well-suited for applications requiring fast and accurate computations, such as real-time control of robotic arms in space. SPART also includes tools for analyzing the workspace and kinematic manipulability of manipulators, critical for optimizing configurations for tasks such as object capture or satellite servicing. Additionally, it incorporates pre-built controllers for executing

advanced maneuvers, like the Zero Reaction Maneuver (ZRM), which minimizes unwanted reactions on the spacecraft base. Compared to other tools, SPART stands out due to its direct access to kinematic and dynamic parameters, compatibility with embedded hardware, and its specific focus on floating-base systems in space. By simplifying development and enabling rapid prototyping, SPART makes space robotics more accessible, supporting advancements in complex missions like debris removal, satellite servicing, and autonomous docking.

Another recent project is POSEIDYN [23], is an advanced test bed designed for the experimental development and validation of guidance, navigation, and control (GNC) systems for spacecraft engaged in proximity maneuvers. It plays a pivotal role in simulating critical scenarios such as rendezvous and proximity operations in a near-frictionless environment, enabling realistic and precise testing.

Its importance lies primarily in its ability to support the development of advanced autonomous GN&C algorithms. By providing a controlled and representative platform, POSEIDYN enables researchers to design, test, and refine algorithms essential for complex spacecraft missions, such as orbital maintenance, autonomous docking and planetary exploration.

The test bed offers a highly realistic environment thanks to its granite monolith, which ensures a leveled and nearly frictionless surface. This, combined with air bearings, allows for accurate replication of translational and rotational motions. Furthermore, the system integrates state-of-the-art technology, including fiber-optic gyroscopes and motion capture systems, for precise positional and orientational data, as well as cold-gas thrusters and reaction wheels to simulate actual spacecraft dynamics.

POSEIDYN's modular software architecture enhances its flexibility, allowing tailored testing for navigation, guidance, and control research. The compatibility with development tools like MATLAB/SIMULINK simplifies the transition of models from simulation to physical testing. Its design also addresses crucial challenges in mission planning, such as optimizing trajectories to balance safety and fuel efficiency, the key for long-duration missions.

Within the realm of FSS, POSEIDYN stands out as a cutting-edge platform. It is indispensable for advancing technologies required for rendezvous, docking, and in-orbit maintenance, offering a significant edge over similar test beds in its precision and adaptability. This makes it a cornerstone in the development of innovative solutions for increasingly demanding space missions.

As it is possible to see, the key component of this type of simulator is the matching plane, which represents the most significant portion of the installation cost due to substantial expenses associated with transportation and assembly. A critical characteristic of the matching plane is its flatness, defined as the maximum permissible deviation from a perfectly flat surface. This parameter is essential in applications that require extreme precision, such as simulators designed for space
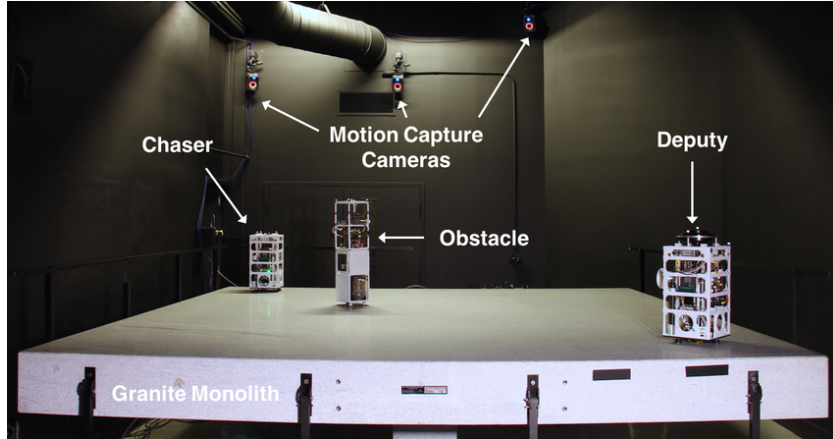
Figure 2.6: PoseiDyn FSS at NPS [23]

experiments. Flatness is typically expressed in length units, often in micrometers (µm) and it depends only on the length of the longer side of the plane. In the context of space simulation, the flatness requirements are particularly stringent, generally ranging from 3 µm for smaller planes to 46 µm for bigger planes [24], contingent on the specific experimental requirements and design parameters.

The materials commonly utilized to construct high-precision passive floors include glass, epoxy resin, and granite[18]. While glass and epoxy resin facilitate the creation of expansive floor surfaces advantageous for experiments that necessitate a large operational area, they exhibit lower flatness tolerances compared to granite. Consequently, these materials are less suited for applications demanding exceptional precision. In contrast, granite provides superior dimensional stability and exceptional flatness due to its inherent strength and structural homogeneity.

It is possible to create larger testbed platforms by combining multiple matching planes, but this approach comes with significant challenges compared to a single surface made from one piece of material [8]. Surface discontinuities at the joints between panels cannot be entirely avoided, leading to local deterioration of surface parameters that may negatively influence the performance of air bearings during tests. In addition to using multiple smaller granite plane united to create a larger surface, one other solution could involve two separate granite planes with 2 or more communicating FSS. However, leveling the entire testbed surface in such configurations becomes significantly more complex, as it requires not only ensuring the planarity of both granite planes but also making sure they are aligned at the same level relative to each other.

---

[1]Multiple panels could be used to obtain larger surface.

Surface material	Surface size	Surface roughness	Surface flatness	Surface levelling
Granite	Small to medium[1]	Low	High	Adjustable legs, possibility of surface tilting to simulate low-g conditions
Glass	Small[1]	Low	High	Adjustable legs, possibility of surface tilting to simulate low-g conditions
Epoxy	Medium to large	Moderate	Moderate	Levelled surface obtained during construction process, no adjustable legs

Table 2.1: Most common surface materials for planar air-bearing microgravity simulators [8]

In the European context, the flatness of granite is governed by the DIN 876 standard, which delineates the flatness error (or tolerance) as the deviation from an ideal plane equidistant from two parallel planes that contact the highest and lowest points of the examined surface. This definition, as illustrated in fig. 2.7 , offers a metrological basis for quantifying deviations from perfect flatness.
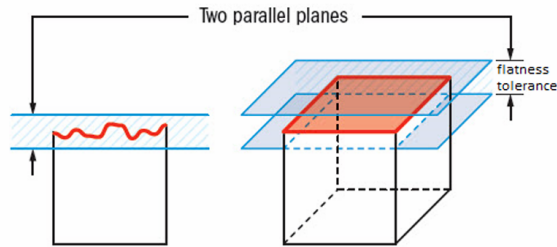
Figure 2.7: Flatness Tolerance [25]

The DIN 876 standard classifies flatness into five distinct grades, each corresponding to specific flatness tolerances required for various applications. As outlined in Table 2.2, these grades range from Grade 000, which represents the highest level of precision, to Grade 3 [26], which denotes the least precise standard. This classification serves as a critical resource for engineers and designers, providing essential guidance in determining the requisite flatness specifications tailored to the particular demands of each application. By adhering to these established grades, professionals can ensure that the materials and surfaces utilized meet the necessary performance criteria for their intended use.

Grade	Tolerance [μm]
000	$1\left(1 + \frac{L}{1000}\right)$
00	$2\left(1 + \frac{L}{1000}\right)$
0	$4\left(1 + \frac{L}{1000}\right)$
1	$10\left(1 + \frac{L}{1000}\right)$
2	$20\left(1 + \frac{L}{1000}\right)$
3	$40\left(1 + \frac{L}{1000}\right)$

Table 2.2: DIN 876 grades of flatness.
L = longest side of the floor in [mm]

In Table 2.3 additional information on existing testbed installations to provide a point of comparison with this thesis work is provided.

Main Research Topics	DOF	Material	Size [m²]	Year	Location	Institution
Free floating satellite-manipulator systems	3	Glass	1.8 × 1.8	1990	Japan	Tokyo Institute of Technology [27]
Satellite formation flying and proximity operations	6	Glass	1.5 × 7.3 (panels?)	2001	USA	Lawrence Livermore National Laboratory [28]
Control of a flexible manipulator	Fixed base	Glass	2 × 2	2004	Italy	University of Pavia [29]
Manipulator hardware testing	Fixed base	Granite	4.2 × 3.6 (panels)	2006	China	Harbin Institute of Technology [30]
Docking	3	Granite	1.93 × 1.52	2006	Canada	MDA Space Missions [31]
Satellite formation flying and proximity operations	3	Granite	2.74 × 3.66	2006	USA	Stanford University [32]
Free floating satellite-manipulator systems, flexible structures	3	Granite	1.3 × 2.2	2008	USA	Massachusetts Institute of Technology [33]
Free floating satellite-manipulator systems,flexible structures, satellite formation flying	3	Epoxy floor	Octagon with $d = 5.1$	2008	USA	MIT [33]
Free floating satellite-manipulator systems	3	Granite	2 × 1.8	2008	Greece	National Technical University of Athens [34]
Satellite formation flying and proximity operations	5	Metal panels	7.3 × 8.5 (14 panels)	2008	USA	Jet Propulsion Laboratory [35]
Satellite formation flying and proximity operations	5	Epoxy floor	3.66 × 3.66	2009	USA	Georgia Institute of Technology [36]
Free floating satellite-manipulator systems, docking	3	Marble	1 × 1	2010	Japan	Tohoku University [37]
Satellite formation flying and proximity operations	5	Epoxy floor	4.9 × 4.3	2010	USA	Naval Postgraduate School [38]
Satellite formation flying and proximity operations	6	Granite	4 × 2.5	2010	Germany	DLR, Institute of Space Systems [39]
Free floating satellite-manipulator systems, landing gears	3	Granite	2 × 3	2013	Poland	Space Research Centre (CBK PAN) [40]
Satellite formation flying and proximity operations	6	Epoxy floor	3.96 × 4.57	2013	USA	Rensselaer Polytechnic Institute [41]
Satellite formation flying and proximity operations	3	Granite	4 × 4	2018	USA	Naval Postgraduate School [42]
Satellite formation flying and proximity operations, GNC alghoritm testing	3	Granite	0.4 × 0.6	2023	Italy	Politecnico di Torino [24]

Table 2.3: Summary of notable air-bearing testbeds based on their main research topics, DOF, construction material, size, year of establishment, location, and institution. [8]

17

Starting from the data in Table 2.3 is it possible to make a statistical analysis to investigate the correlation between different factors such as the testbed material and the DOFs.
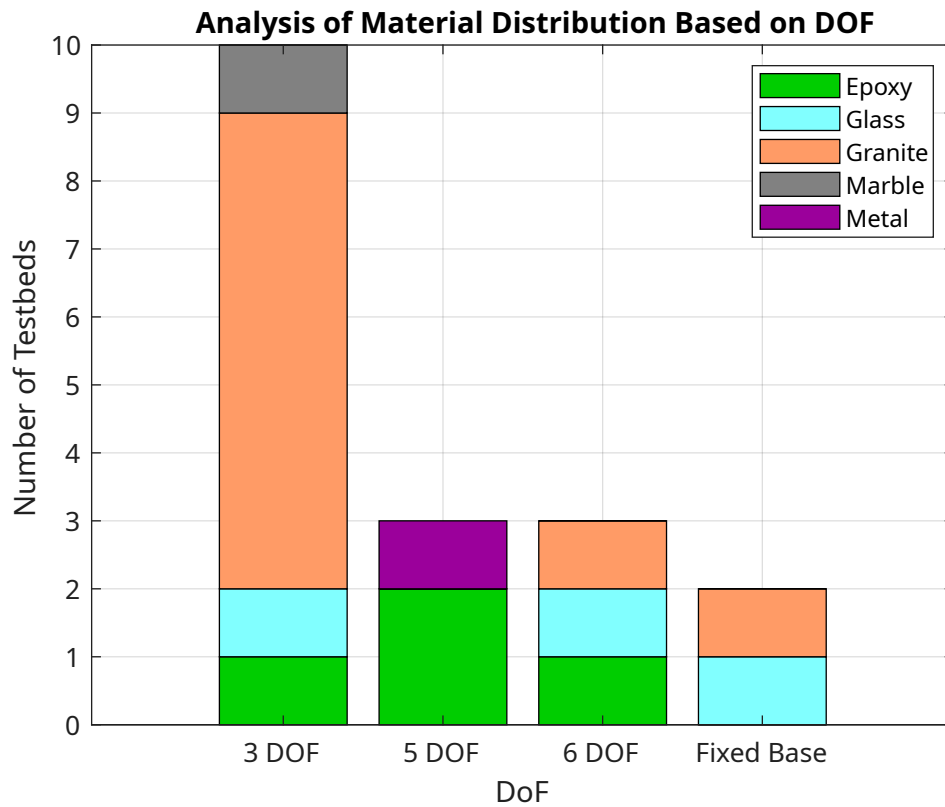
Figure 2.8: Analysis of material distribuition based on DoF
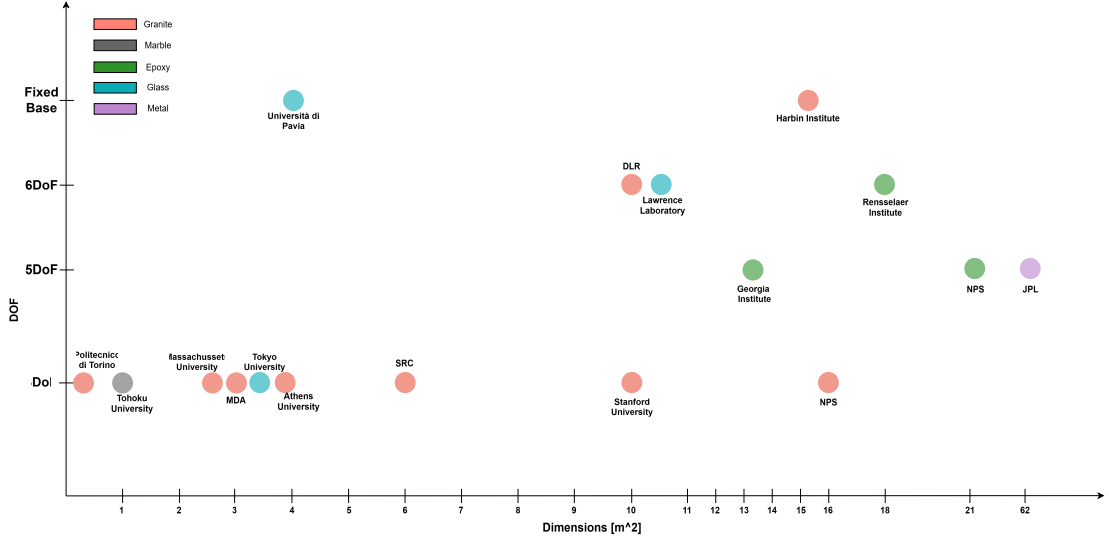
Figure 2.9: Statistical analysis of correlation between dimensions, DoF and material

As it is possible to see in Figure 2.8 and Figure 2.9 granite testbeds are commonly used for 3 DOF applications, whereas epoxy ones are used for 5/6 DOF applications. Metal is used for bigger testbeds applications. These informations could be extremely important for considerations about the testbed to match the FSS designed in this thesis.

One of the significant advancements in HIL testing technology is the incorporation of a dynamically tilting plane, which enhances the simulation of orbital dynamics for spacecraft. The tip-tilt HIL air-bearing testbed is designed to physically emulate the dynamics of spacecraft in orbit by tilting a planar granite surface, effectively replicating orbital forces and trajectories. This innovative approach provides a more realistic and controlled environment for testing spacecraft performance and navigation algorithms.

The testbed features a precision-engineered granite table, supported by three points:

- Central Support (Point P0): This central support acts as a hinge, allowing the table to rotate around two axes, thereby enabling tilting motion in multiple directions.

- Lateral Supports (Points P1 and P2): Known as Motion Support Actuators (MSAs), these supports move along the vertical axis, providing dynamic adjustments of the table's incline. Equipped with spherical hinges, they allow for independent motion, accommodating variations in height and facilitating precise control of the table's tilt.
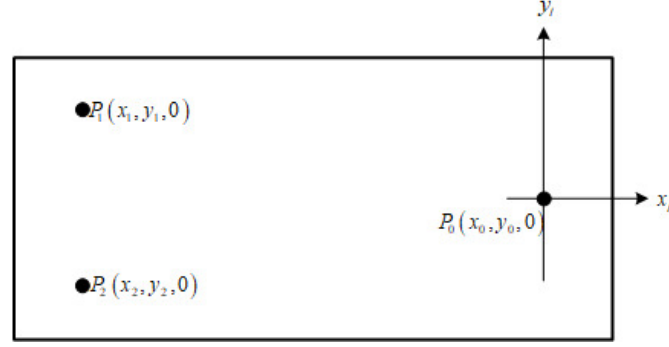
Figure 2.10: Granite table on three points of support P0, P1 and P2 in horizontal configuration [43]

The MSAs dynamically modify the table's orientation along its pitch and roll axes, enabling the Earth's gravitational acceleration to act as a surrogate for orbital forces. This mechanism eliminates the need for the test vehicle's onboard thrusters to simulate orbital motion.

Traditional granite-based testbeds simulate microgravity environments on a leveled planar surface, relying on the test vehicle's onboard actuators to generate orbital dynamics. This approach mixes control and orbital simulation, often introducing inaccuracies such as thruster misalignments and reduced fidelity in replicating true space conditions. The tip-tilt testbed addresses these limitations by decoupling the simulation of orbital dynamics from the test vehicle's propulsion system. Instead of relying on onboard thrusters, the system employs dynamically tilting surfaces to emulate orbital acceleration due to the change in the gravity gradient to which the FSS is subjected. By changing the gravity gradient experienced by the FSS by tilting the table, it is possible to simulate the disturbances of the orbital dynamics.

The tilting is controlled by pre-computed displacements of Mechanical Screw Actuators (MSAs), which adjust the granite table's orientation based on scaled Clohessy-Wiltshire (CW) dynamics. By leveraging gravitational forces through surface tilting, the testbed provides a more accurate and interference-free representation of orbital motion. This clear separation between orbital simulation and control tasks ensures that the test environment is not affected by propulsion-related disturbances, enabling more reliable experiments.

As a result, whereas conventional air-bearing testbeds are limited to short-range proximity maneuvers due to the absence of emulated orbital dynamics, the tip-tilt testbed overcomes this limitation by enabling the simulation of longer and more complex orbital trajectories. Through its dynamically inclined surface, the system replicates relative orbital motion, supporting extended-duration scenarios such as formation flying, rendezvous, and proximity operations.

The functionality of the tip-tilt testbed is underpinned by scaling laws derived from Buckingham's Pi theorem and the similarity principle, ensuring that the dynamics of the scaled FSS accurately mirror those of real spacecraft. This dimensional consistency preserves critical relationships among velocity, acceleration, and force, ensuring that results are applicable to real-world missions. By tilting the table, the testbed creates gravitational accelerations that replicate orbital forces with high fidelity, enabling the reproduction of linearized CW dynamics and potentially nonlinear models within planar motion constraints.

The MSAs provide sub-millimeter accuracy and repeatability, allowing precise adjustments to the table's orientation. Real-time computer control translates required accelerations into actuator commands, dynamically tilting the table to follow the scaled CW dynamics. Using a navigation system, is it possible to improve performance by continuously monitoring the FSS's position and velocity, enabling closed-loop adjustments. Each operational cycle, including sensing, processing, and actuation, completes in less than 1 second [44], ensuring real-time responsiveness.

Comparison between reduced gravity simulators

Although parabolic flights and fall towers may seem similar at first glance, each offers unique advantages and disadvantages that must be carefully considered depending on the specific requirements of the experiment. Additionally, FSS present an alternative approach for achieving microgravity-like conditions, adding further versatility to the options available for testing.

Parabolic flights provide significant benefits, particularly in the form of longer microgravity durations, typically lasting between 20 to 25 seconds per parabola, which is nearly double the duration offered by fall towers. Furthermore, the aircraft's cabin provides ample space, accommodating larger experimental setups and more complex systems. However, the very nature of parabolic flight introduces external disturbances, such as lift, drag, and thrust variations, which hinder the creation of perfect microgravity conditions. These forces, combined with engine vibrations and the unusual maneuvering of the aircraft, result in microgravity fluctuations of approximately ±0.05g at a frequency of about 1Hz[10]. Additionally, parabolic flights are subject to inherent inconsistencies, with small variations between parabolas making it difficult to achieve perfectly uniform testing conditions. These limitations are compounded by the high costs associated with such flights and the challenges of scheduling, which often restrict accessibility.

Fall towers, by contrast, offer a more cost-effective and straightforward alternative. These facilities enable highly reproducible testing, with experiments conducted under consistent conditions, as the drop sequence remains identical for each test. The lower operational costs make fall towers particularly attractive for frequent, iterative experimentation. However, the microgravity duration is significantly

shorter, typically lasting only 2 to 10 seconds, which may be insufficient for some experiments. Moreover, the size and weight of the experiments are restricted by the dimensions of the drop capsule and the physical constraints of the facility itself, limiting their versatility compared to parabolic flights[16].

Free Space Simulators (FSS) provide another approach to simulating microgravity, often employing technologies such as air-bearing platforms or suspension systems. These simulators are particularly valuable for small-scale robotics and spacecraft component testing. One of their primary advantages is the ability to support longer test durations, often extending to several minutes or even hours, which is not feasible with fall towers. Additionally, FSS facilities allow for high repeatability, enabling experiments to be conducted under identical conditions, which is critical for refining designs and validating performance. Cost efficiency is another benefit, as these systems are generally less expensive to operate than parabolic flights and are more readily available for frequent use. However, the size of experiments is again a limiting factor, as these simulators can typically support only lightweight equipment. Furthermore, FSS often simulate microgravity along specific axes rather than providing a complete, omnidirectional microgravity environment, which may restrict their application for certain experiments requiring full six-degree freedom.

In summary, each method presents distinct strengths and weaknesses, making them suitable for different types of experiments. Parabolic flights are ideal for larger, more complex setups requiring longer microgravity durations, although at a higher cost and with certain physical disturbances. Fall towers offer a cost-effective, highly reproducible solution for smaller-scale experiments, though they are constrained by shorter durations and size limitations. FSS provide a balance, allowing for extended testing and repeatability at a lower cost, but are limited to smaller experiments and partial microgravity simulation. The choice of method ultimately depends on the specific objectives and constraints of the experiment, such as required microgravity duration, precision, budget, and equipment size.

It is possible to summarize the main advantages and disadvantages of all three types of reduced gravity simulators in terms of costs, microgravity duration, availability and test dimension in Table 2.4.

	Cost [$]	Microgravity duration [s]	Availability	Test dimension [m]
Parabolic flight	10300-295000	20	Up to 2 tests/day	Up to 20m long
Fall tower	>20000	< 10	Up to 3 tests/day	Up to 1.8 m long
FSS	<20000	>60	>10 tests/day	< 1m long

Table 2.4: Parabolic flight, Fall tower and FSS comparison in terms of cost, test duration, availability and test dimension

Chapter 3

Floating Spacecraft Simulator Preliminary Design

3.1 Introduction to Systems Engineering

Systems Engineering (SE) is an interdisciplinary approach that provides a structured methodology for managing, designing and analyzing the lifecycle of a product. This approach relies on a well-defined process and employs specific graphical representations to ensure clear communication and a comprehensive understanding of the system's functions and requirements. Among the most commonly used tools there are block diagrams, such as the functional tree and the functional diagram, but also other significant tools like the N2 matrix and the functions/products matrix. These tools play a crucial role during the preliminary design phase, enabling the identification of system requirements and guiding the selection of components that best meet those requirements.

SE is structured around the V-Model, a development framework that systematically outlines the phases of the design and verification process of a system. In this chapter, we focus on the initial phases of the left branch of the V-Model, which corresponds to the Verification Phase as shown in Figure 3.1. These phases encompass the analysis of requirements, the definition of the system's primary functions, and the creation of a solid foundation for the preliminary design of the FSS. The goal is to establish a structured project where requirements are clearly defined, ensuring that the system can be effectively verified.

Building upon SE, Model-Based Systems Engineering (MBSE) has emerged as a significant innovation in the field. MBSE extends the traditional approach by

incorporating the creation of detailed models using specific software tools, enabling a more analytical and comprehensive representation of the system. One widely used example of such tools is SysML (Systems Modeling Language), a standardized language specifically designed to support MBSE methodologies [7]. SysML provides a framework for developing and visualizing system models, covering aspects such as requirements, behaviors, structures and interactions. This model-based approach not only enhances the understanding of interactions between components but also makes managing system complexity more efficient, thanks to its capacity for dynamic simulation and validation of the design.
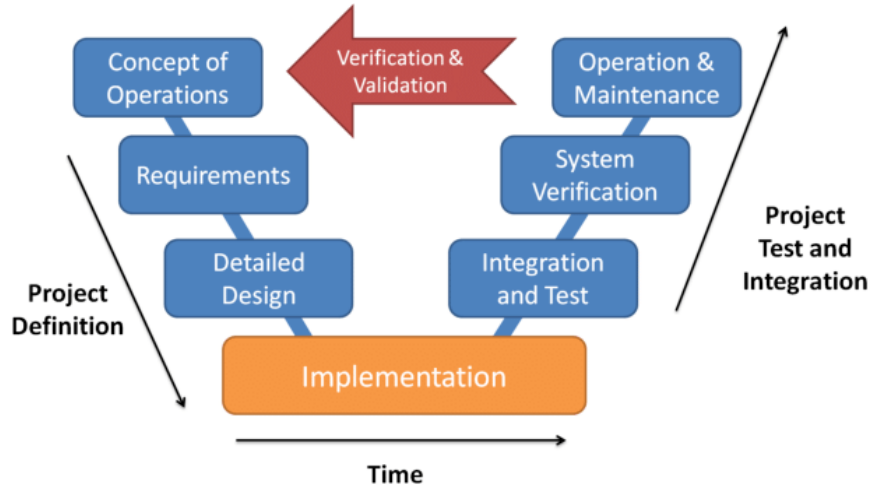
Figure 3.1: System Enginering V-Model [45]

3.2 The importance of the AI implementation

The increasing application of Artificial Intelligence (AI) has significantly impacted the space sector, offering potential improvements in both accuracy and computational efficiency. For the purpose of this thesis, which focuses on a simulator for the test of algorithms for rendezvous and docking maneuvers, the key AI technologies at play are primarily deep learning and reinforcement learning.

Preliminary tests have already been conducted, examining trajectory optimization problems in major missions such as Cassini 2 and Messenger [46]. In each studied case of this analysis it was found that the application of standard global optimization solvers such as Differential Evolution(DE), Particle Swarm Optimisation(PSO), Genetic Algorithm(GA) and Simulated Annealing(SA), was insufficient for finding optimal solutions, suggesting the need for more advanced methods like a collaborative method between these solvers. Other future improvements could

be obtained by using the Guidance and Control Networks (G&CNETs) [42] which are general deep architectures trained to perform optimal maneuvers via imitation learning. These networks could introduce a novel approach using differential algebra and automated differentiation to evaluate their stability margins and control performance. G&CNETs, therefore, represent one of the most promising deep learning-based technologies, with the potential to simplify onboard control and guidance systems by replacing them with a relatively simple, trained neural model.

Reinforcement Learning (RL), a subfield of machine learning in which agents learn to solve tasks such as navigation or planning in dynamic environments, is also expected to see significant advancements in the future. One of the key advantages of RL is its ability to adapt to unpredictable situations and circumstances that are difficult to foresee or cumbersome to manage manually. As a result, autonomous navigation and control challenges, where uncertainty and robustness are paramount, are ideal candidates for RL applications. Typical challenges in this domain include controllers that enable spacecraft to hover and orbit irregularly shaped bodies, such as asteroids. Litterature [47] has demonstrated that RL can learn the non-uniform gravitational and rotational fields of simulated asteroids to develop thrust profiles for accurate and robust hovering. This task would otherwise be extremely time-consuming to solve using traditional methods, considering the wide variety of asteroid shapes found within our solar system.

So in conclusion, the implementation of this kind of technology in the FSS would permit the FSS to perform autonomous simulation of space maneuvers, adapting to potential perturbations without human intervention, such as trajectory adjustments due to external factors and then, after extensive testing, it could be used to predict the necessary maneuvers based on initial input data with the potential use of neural network.

Obviously there are also drawbacks, first of all AI operates as a black box, this means that the reasoning behind its computations is not fully transparent, so this could lead to initial errors, which may then propagate and affect subsequent tests. It should also be taken into account that AI is not deterministic, this means that the same inputs may result in different outputs.

3.3   System Definition and Concept of Operations

To establish a preliminary high-level system definition and concept of operations for the FSS, it's crucial to incorporate visual elements that can enhance more clarity and understanding.

In particular, the functional tree, shown in Figure 3.2, is a breakdown of macrofunctions, where each high-level function is decomposed into its primary components. As we move downward in the tree, we answer the question "how?",

exploring how the functions are carried out by specific components. Conversely, moving upward answers the question "why?", providing the reasoning behind performing these functions. The lowest-level functions must be carried out by specific products, fulfilling the required tasks to complete the overall functionality. Starting from Figure 3.2 it is possible to define the functions/products matrix shown in Figure 3.3, this matrix links the function to the product capable of performing that function.
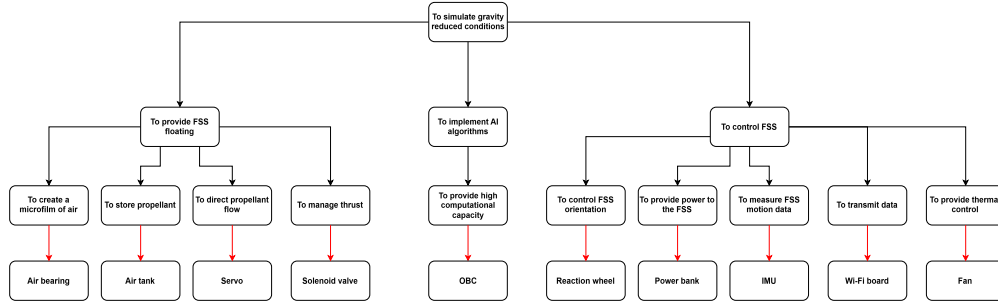
Figure 3.2: Functional tree with products

Figure 3.3: Functions/products matrix

Subsequently, in Figure 3.4 the operational flowchart is presented. The operational flowchart served as the basis for identifying system requirements and playing an important role in defining a preliminary power budget once specific components are chosen. It outlines the operational modes of the FSS, showing what different systems are utilized in each mode. Each block represents a distinct mode of operation, with transitions between these phases reflecting changes in the system state. In the initial **Stand-By Mode**, the simulator is at idle and only basic systems like the OBC, EPS, and TCS are operational to maintain minimal functionality. The Communication System is active to be able to send instructions to the simulator. During the **Calibration Mode** the simulator ensures that its orientation, sensors, and actuators are properly configured. The ADCS is crucial in this phase to gather orientation data. Next an **Operative Mode** is defined where the simulator is fully operational and performs the primary simulation tasks. The Propulsion becomes active to start the floating phase of the FSS, simulating microgravity maneuvers while the OBC is performing at its maximum capabilities to iteratively run the simulation algorithms. At this point two different cases are considered. If the simulation is going smoothly and correctly the simulator enters in a **Post-Operative Stand-By Mode**. Otherwise a **Failure Mode** is activated triggered when an error or malfunction is detected in the system. The simulator enters a safe mode, likely deactivating non-essential systems while retaining minimal functionality to diagnose the issue and communicate its status. The OBC may attempt recovery actions or send alerts to external monitors via the COMM system. At the end of the experiment a **Shut Down** is performed allowing for recharging operations, data collection and analysis and if necessary, recovery of the system.
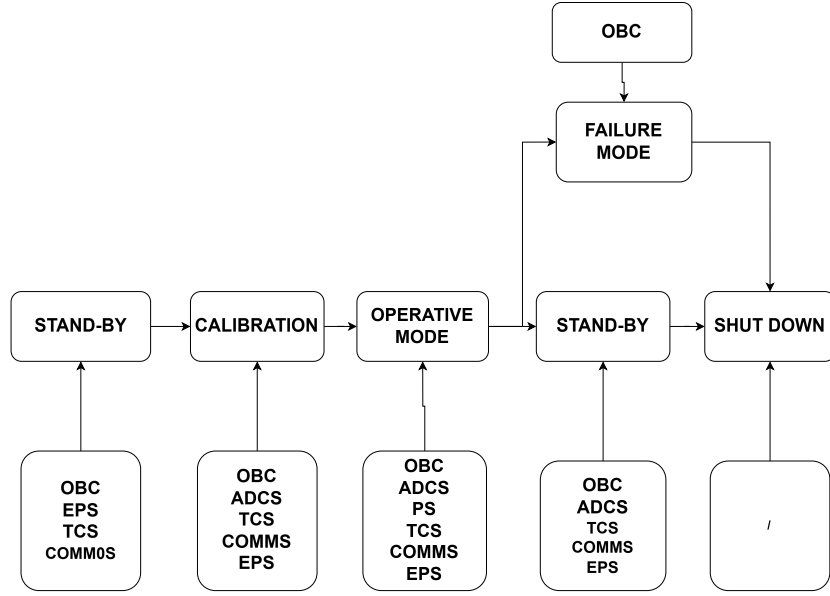
Figure 3.4: Operative modes flowchart with active subsystems for each mode

Another diagram commonly used in the SE methodology is the N2 diagram, which follows ECSS standards too and is used to represent and analyze the interactions between different components of a complex system in order to have a better understanding of system integration.

As it is possible to see in Figure 3.5, the N2 diagram consists of a square matrix, where only the upper triangular portion is considered. The diagonal cells represent the system components, whereas the off-diagonal cells indicate interactions between them, which in this specific case can be electrical, mechanical, pneumatic, or data transfer-related.
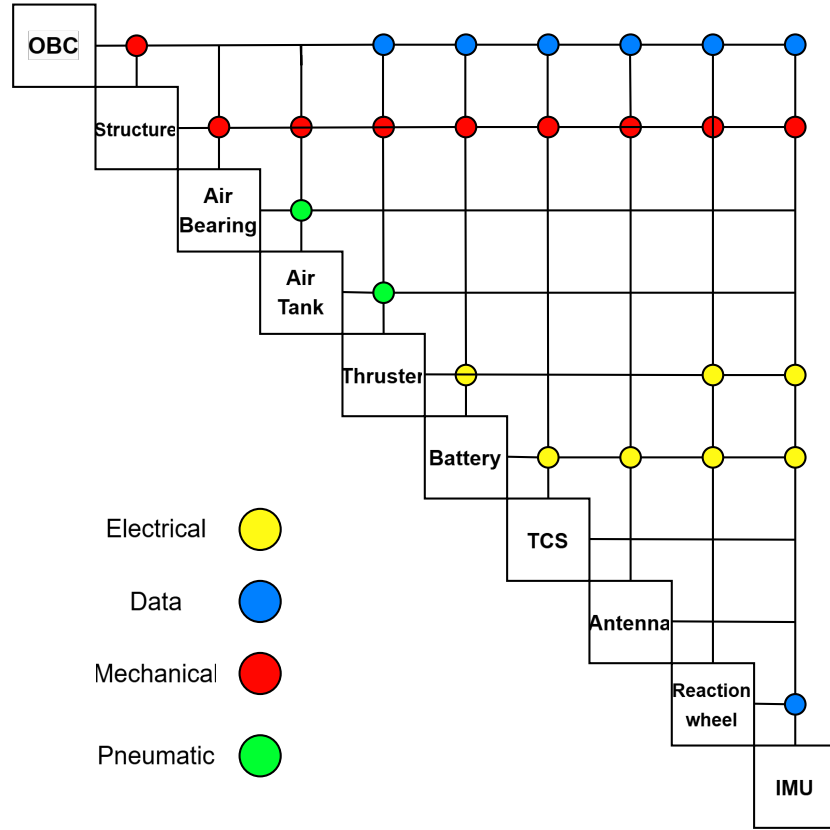
Figure 3.5: N2 diagram of the FSS main components

3.4   Approach to the project

Before diving into the core of the preliminary design, it is essential to define a set of guiding principles that will be followed throughout the project. For this thesis, five key guidelines have been defined, serving as the foundation for the preliminary design in the following sections:

1. **AI Integration**:The primary objective of this project is to develop a preliminary design that can effectively support the implementation of artificial intelligence.

2. **System Modularity**: Ensuring modularity is crucial not only for the versatility and adaptability of the system but also for guaranteeing the reliability of future test results. Specifically, to maintain accuracy, the center of mass of the Floating Spacecraft Simulator (FSS) must align with that of the reference satellite.

3. **Reduction of System Complexity**: simplifying the system's design is essential to facilitate the later stages of integration.

4. **Utilization of Pre-Existing Components whenever possible**: components previously used in similar applications should be incorporated. This approach accelerates development and integration while maintaining high reliability.

5. **Weight Reduction**: stands out as an important factor for achieving longer operational phases .

By adhering to these principles, the preliminary design is structured to meet the project's objectives while optimizing efficiency and performance.

Based on literature Analysis [48] and fixed the main guidelines for the development of the preliminary design, it is possible to define the system requirements. This step is crucial because the requirements act as a bridge between the high-level functions outlined in Figure 3.2 and the detailed design of the system focusing more on the choice of specific components. By establishing clear and precise requirements, it is possible to validate the solutions chosen, ensuring that the system's specific functions are correctly implemented facilitating the transition from concept to realization and testing.

Starting from the OBC, it is possible to define the following requirements in Table 3.1 based both on the information available in the literature regarding the typical specifications of the most commonly used boards for AI applications [49][50] [51]. In particular from the requirements stated by Microsoft in [52] is it possible to fix the minimum requirements for the choice of the OBC in order to have a solid foundation for the subsequent trade off analysis.

ID	Requirement	Verification Method
OBC-01	The On Board Computer shall provide a computing performance of at least 40 Tera Operations per Second for AI workloads.	Performance Benchmark
OBC-02	The On Board Computer shall be equipped with a minimum of 16GB of RAM to ensure adequate performance.	Performance Benchmark
OBC-03	The On Board Computer shall support at least a 4-core CPU.	Performance Benchmark
OBC-04	The On Board Computer shall include a GPU or AI accelerator with at least 128 CUDA cores or AI-specific cores.	Performance Benchmark
OBC-05	The On Board Computer shall support wireless communication through integrated Wi-Fi or Bluetooth.	Compatibility and Software Test
OBC-06	The On Board Computer shall include a minimum of one USB 3.1 Type-A port for external device connectivity.	Compatibility and Software Test
OBC-07	The On Board Computer shall operate within a power envelope configurable up to 30W.	Electrical Test
OBC-08	The On Board Computer shall include pins to connect to other system components.	Compatibility and Software Test

Table 3.1: OBC Requirements

Then it is possible to define the requirements for the Propulsion System as reported in Table 3.2 according to the data acquired by others similar applications seen in the previous chapter.

ID	Requirement	Verification Method
PS-01	The PS tank shall have a capacity of at least 0.2 L.	Datasheet verification
PS-02	The PS shall be able to direct the flow in the desired direction.	Pneumatic test
PS-03	The PS shall guarantee the correct operative input pressure for each pneumatic component.	Pneumatic test
PS-04	The PS shall guarantee an autonomy of at least 20 minutes	Experimental test

Table 3.2: Propulsion System Requirements

For ADCS we can identify the following requirements in Table 3.3 obtained from documented experiments of other FSSs present in the literature.[53].

ID	Requirement	Verification Method
ADCS-01	The ADCS shall measure acceleration along 3 axes (X, Y, Z) with a range of at least 2g.	Dynamic Testing + Environmental Testing
ADCS-02	The ADCS shall measure angular velocity along 3 axes with a range of at least 100° degrees per second (°/s).	Dynamic Testing + Environmental Testing
ADCS-03	The ADCS shall include a 3-axis magnetometer for measuring the Earth's magnetic field with a range of at least ±2 gauss.	Dynamic Testing + Environmental Testing
ADCS-04	The ADCS shall provide an angular rate resolution of at least 0.005°/s.	Dynamic Testing + Environmental Testing
ADCS-05	The ADCS shall have an accelerometer resolution of less than $0.05 \ 10^{-3}$g.	Dynamic Testing + Environmental Testing
ADCS-06	The ADCS shall provide data with data transmission latency of less than $2 \ 10^{-3}$s.	Dynamic Testing + Environmental Testing
ADCS-07	The ADCS shall be resilient to vibrations up to 4 g over a frequency range of 20 Hz to 2 kHz.	Dynamic Testing + Environmental Testing
ADCS-08	The ADCS shall provide error detection and correction for data transmission.	Dynamic Testing
ADCS-09	The ADCS shall be capable of providing an angular momentum of at least 1 mNms.	Datasheet verification

Table 3.3: ADCS Requirements

Moving to EPS, the requirements in Table 3.4 can be established to guarantee the correct functioning of the simulator during all the experiment phases. Also in this case, the requirements are derived by data acquired by similar applications:

ID	Requirement	Verification Method
EPS-01	The EPS shall provide a minimum total energy capacity of 16 Ah	Electrical Test
EPS-02	The EPS shall provide a regulated DC output voltage of 12 V and 5 V for different subsystems.	Electrical Test
EPS-03	The EPS shall support a peak output current of at least 4 A	Electrical Test
EPS-04	The EPS shall achieve a power conversion efficiency of at least 85% during voltage regulation.	Electrical Test
EPS-05	The EPS shall support fast charging with an input power of at least 20W.	Electrical Test
EPS-06	The EPS shall include protection against overcurrent, overvoltage, and short circuits.	Electrical Test
EPS-07	The EPS shall support easy replacement of battery modules	Electrical Test
EPS-08	The EPS shall guarantee the correct operative voltage for each component	Electrical Test

Table 3.4: EPS Requirements

The Table 3.5 provides the required specifications for TCS which in this case are mainly referred to the systems that are at more risk of overheating during specific phases of the operations, in this specific case the OBC.

ID	Requirement	Verification Method
TCS-01	The TCS shall guarantee an operative temperature of the OBC between -25°C to +60°C.	Thermal Chamber Testing + Sensor Calibration
TCS-02	The TCS shall maintain the battery in an operative temperature range of [0°C, +45°C] during charge mode.	Charge/Discharge Testing + Thermal Profiling
TCS-03	The TCS shall maintain the battery in an operative temperature range of [-20°C, +60°C] during discharge mode.	Charge/Discharge Testing + Environmental Stress Screening

Table 3.5: TCS Requirements

The requirements in Table 3.6 are necessary for the Communication System based on the functional tree and the main necessity for correct functioning of the simulator:

ID	Requirement	Verification Method
CS-01	The Communication System shall support Wi-Fi connection	Interface Testing
CS-02	The Communication System shall collect raw data from various subsystems through OBC	Interface Testing
CS-03	The Communication System shall provide connection over a range of at least 20 meters.	Interface Testing

Table 3.6: Communication System Requirements

3.5   Systems Overview and Description

As shown in Figure 3.2 and Figure 3.5 the FSS is composed of several interconnected components that work together. This section delves into a more detailed functional analysis of each subsystem, which led to the selection of the components using the **Analytic Hierarchy Process (AHP) method** arriving to a detailed design of the FSS and resuming it with a CAD assembly of all the components. The AHP method is a key tool in the SE approach, based on identifying Figures of Merit (FoM) to conduct trade-off analyses. It allows for comparing different options for each subsystem to determine the one that best fits the project requirements. Specifically, in this project, the following FoMs have been taken into account:

- **Performance**

- **Maximum power required**

- **Weight**

- **Cost**

- **Modularity**

- **Complexity**

The first step of the AHP method is to define the priority of each FoM, and to do it, each FoM is compared pairwise with others FoMs using a scale from 1 to 9 [54], in Table 3.7 is it possible to see the meanings of these values.

Once the rank for each FoM is obtained, after the normalization of each parameter, it is possible to obtain the prioritization matrix for each option and then define the decision matrix. In the next sections this method has been used for the selection of some subsystems components, since the FoM of the performance is too generic, specific parameters have been used depending on the subsystem.

Value	Importance Level
1	Equal importance
2	Weak or slight importance
3	Moderate importance
4	Moderate plus importance
5	Strong importance
6	Strong plus importance
7	Very strong importance
8	Very very strong importance
9	Extreme importance

Table 3.7: The prioritization values with their meaning [54]

3.5.1   Structure

First of all a primary structure is needed to physically connect all the components of the subsystems. The structure is designed to house the air tank, which is the largest and heaviest component of the system and it also must accommodate all other components and provide a secure connection to the air bearing. To achieve this, a primary hollow square structure shown in Figure 3.6 has been developed. It features holes on the bottom, allowing for a stable connection to the air bearing. As shown in Figure 3.7 outer surface of the tank container includes vertical slides designed to accommodate the inserts for the battery, the board and the other components using custom modular cases which an example of is reported in Figure 3.7 highlighting the flexibility and modularity of the design. The entire structure, along with the custom cases have been designed in order to be 3D printed. For the material different choices are available. PolyLactic Acid (PLA) is known for its lightweight yet strong properties and is also widely available and easy to print, providing a balance of strength, ease of use, and affordability. Alternatively, Polyethylene Terephthalate Glycol (PETG) could be used, as it offers greater impact resistance, durability, and heat resistance. It is worth noting that PETG requires slightly more precision in calibration during the printing process and operates at higher printing temperatures. So to make a conservative choice PETG seems the more suitable material for the application in object, providing increased robustness and resistance.
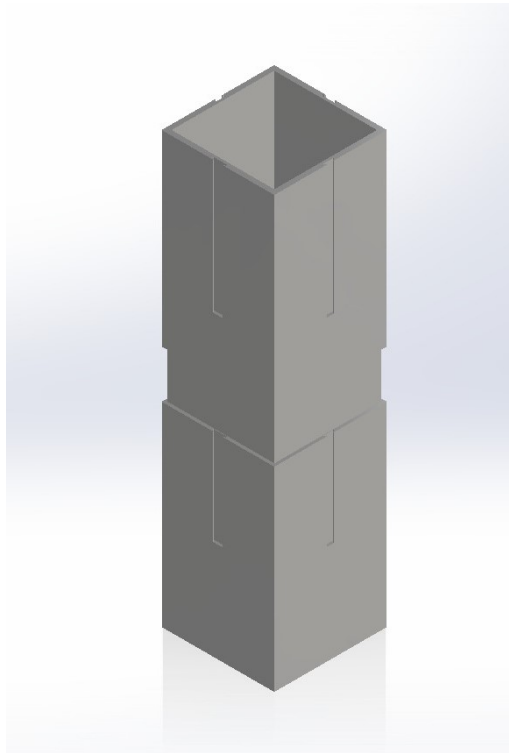
Figure 3.6: CAD of the Structure
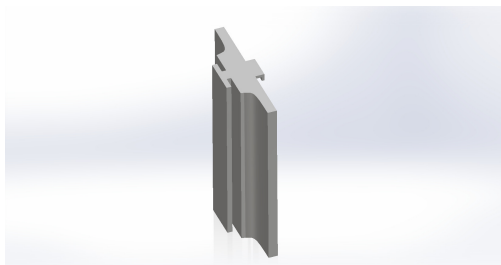
(a) Detail of the case slide
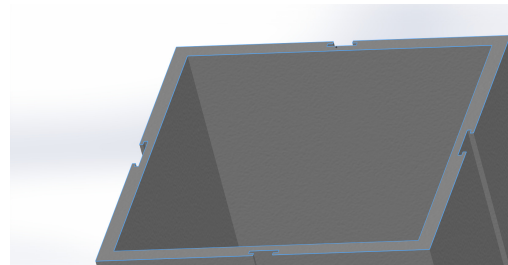
(b) Detail of the structure slide

Figure 3.7: Structure's details

In conclusion, the design choices for the FSS structure focus on balancing functionality, simplicity and ease of manufacturing.
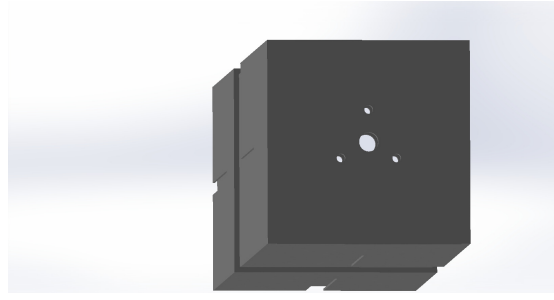
Figure 3.8: Air bearing attach

3.5.2 On Board Computer (OBC)

The on-board computer handles the control of propulsion by managing the servos and solenoid valves, while also running the essential Guidance, Navigation and Control (GN&C) algorithms. It also collects and menages telemetry data coming from on-board sensors

As illustrated in the detailed N2 diagram shown in Figure 3.5, the OBC plays a central role in managing all the subsystems data ensuring coordinated functionality across the system. Starting from the guidelines and Table 3.1 a reserach was conducted to identify the OBCs more suitable for this project. Since there is a direct correlation between the performance of the OBC, its power requirements and the system's weight, the selected OBC should represent an optimal balance among these characteristics. The research highlighted NVIDIA boards as a predominant choice due to their robust performance and widespread adoption in the robotics field. These computers are based on ARM processors and integrate a range of hardware components, such as a CPU, RAM, network connectivity and USB ports along with some general purpose Input/Output pins. Those boards results to be very suitable for this application since are capable of handling complex computations involving real-time processing, machine learning and edge computing[55]. For this first evaluation step all the boards that meet the TOPS requirement were considered:

	TOPS	Power required	RAM	GPU	CPU
AGX Orin 64GB	248	15-60 W	64 GB	2048-core NVIDIA Ampere architecture	12 core Arm Cortex 8.2
AGX Orin 32GB	200	15-40	32 GB	1792-core NVIDIA Ampere architecture	8 core Arm Cortex 8.2
NX Orin 16GB	157	10-40	16 GB	1024-core NVIDIA Ampere architecture	8 core Arm Cortex 8.2
NX Orin 8GB	117	10-40	8 GB	1024-core NVIDIA Ampere architecture	6 core Arm Cortex 8.2
Orin Nano 8GB	67	7-25	8 GB	1024-core NVIDIA Ampere architecture	6 core Arm Cortex 8.2

Table 3.8: OBCs' technical data comparison [56]

Now is it possible to analyze each option using the figures of merit. In this case, since the concept of performance is too generic, the value of Tera Operations Per

Second (TOPS), has been chosen as the parameter to characterize the performance of the OBC.

FOM	AGX Orin 64 GB	AGX Orin 32 GB	NX Orin 16GB	NX Orin 8GB	Orin Nano 8 GB
TOPS	248	200	157	117	67
Maximum power consumption (W)	60	40	40	40	25
Weight (gr)	280	280	182	182	173
Cost (€)	2287	1275	970	605	450

Table 3.9: Preliminary trade-off analysis with figures of merit

Following this, a trade-off evaluation was carried out, considering the minimum hardware requirements outlined in Table 3.1. The first step is to normalize the data of Table 3.9. For those data where a higher value is better is it possible to normalize using the formula:

$$X_{\text{norm}} = \frac{X}{X_{\text{tot}}}$$

On the contrary for those data where a lower value is better the following formula is used:

$$X_{\text{norm}} = 1 - \frac{X}{X_{\text{tot}}}$$

Using the **Analytic Hierarchy Process, AHP, method** it is possible to create a **prioritization matrix** for the Figures of Merit, FoM, that impact on the OBC choice Table 3.10: the performance, the required power, the weight and the cost. This matrix allows also for the determination of the weight of each FoM.

FoM	Performance	Required Power	Weight	Cost	Rank
Performance	1	3	5	7	**0.558**
Required Power	1/3	1	3	5	**0.263**
Weight	1/5	1/3	1	3	**0.122**
Rank	1/7	1/5	1/3	1	**0.057**

Table 3.10: Prioritization matrix of the FoM for the OBC using the AHP method

In Table 3.11 is it possible to see the result of the normalization of the boards.

In conclusion, based on the trade-off data, the optimal solution is the Orin 32 GB. This result meets also the requirements in Table 3.1, so this is the OBC chosen for this thesis work.

	AGX 64	AGX 32	NX 16	NX 8	NANO 8
Performance	0.314	0.253	0.199	0.148	0.085
Power required	0.707	0.805	0.805	0.805	0.878
Weight	0.745	0.745	0.834	0.834	0.842
Cost	0.590	0.772	0.826	0.891	0.919
Total Rank	0.485	**0.487**	0.471	0.447	0.433

Table 3.11: Decision matrix for the OBC using the AHP method
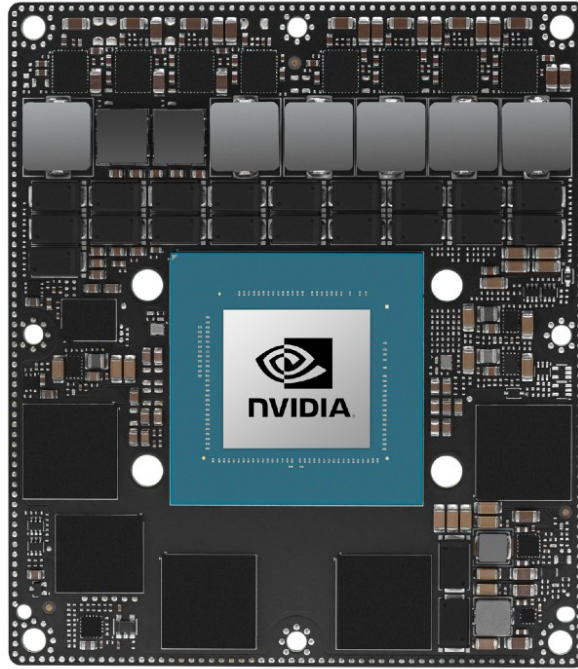
Figure 3.9: Credit: NVIDIA, the NVIDIA Jetson Orin AGX 32 GB [57]

3.5.3 Propulsion System

In the FSS, the propulsion system corresponds to a well-designed pneumatic mechanism, which not only powers the gas thrusters for controlled movement but also supports the air bearings that allow the vehicles to float.

Air bearings work by generating a thin layer of pressurized air between the bearing and the surface. In Figure 3.10 is it possible to see the key concept of the

air bearing functioning. An air film acts as a non-contact interface, eliminating friction and wear while ensuring smooth and precise motion. The pressurized air is introduced through the bearing surface in a controlled manner, creating a stable air cushion that supports the load and allows for high-precision movement.
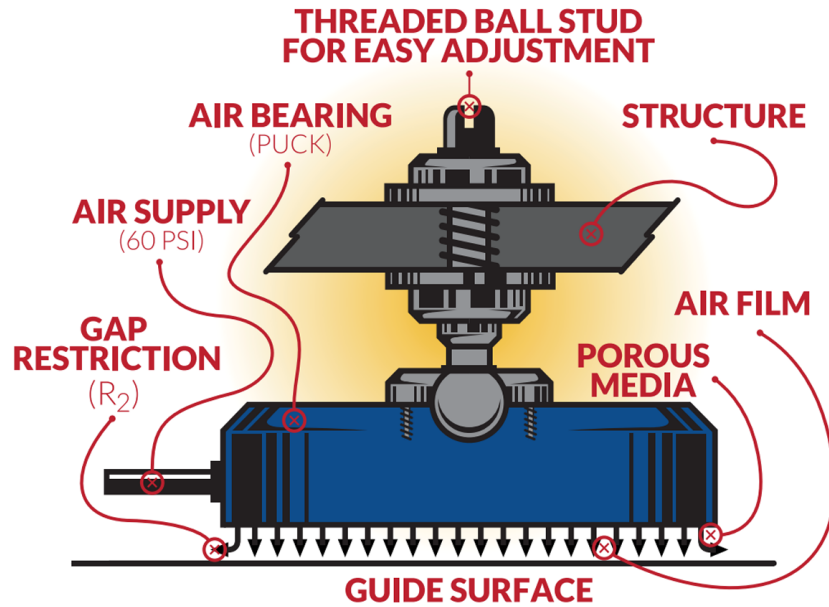
Figure 3.10: Air Bearing Functioning [58]

Air bearings can be classified into two main types: porous media bearings and orifice bearings.

Porous media bearings use a surface composed of millions of microscopic pores to distribute air uniformly across the entire bearing area. These pores restrict the airflow, ensuring even pressure distribution and maintaining a stable air film. This design makes them highly resilient to surface damage or irregularities, as they can continue functioning even if some pores are clogged or damaged. Furthermore, porous bearings are less prone to pneumatic instabilities, such as the "pneumatic hammer effect", which occurs when the air is restricted by a gap slightly smaller than one which allows equilibrium, due to their ability to maintain consistent pressure across the surface.

In contrast, **orifice bearings** rely on precisely placed holes to direct air onto the bearing surface. These holes release the pressurized air, forming a cushion between the bearing and the guide surface. It is also possible to have distribution grooves near to these orifices which help even the pressure distribution profile. While effective, orifice bearings are more susceptible to issues like uneven pressure distribution or damage from scratches near the orifices. In Figure 3.11 different pressure profiles of the air bearings are shown giving a direct meter of comparison

between those.
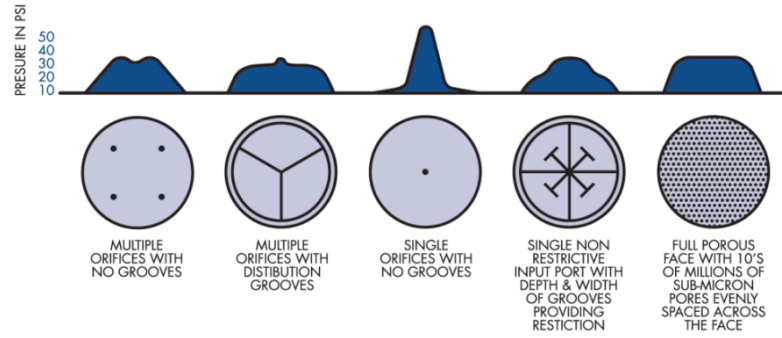
Figure 3.11: Air Bearing pressure profiles [59]

During the design process of the FSS, various configurations of air bearings were considered.

Initially, configurations involving multiple smaller air bearings were evaluated. This approach offered the potential for enhanced stability and distributed load support, but according to the literature[8], the main issue when using multiple air bearings, besides the increased structural complexity of the pneumatic system, is keeping all the bearings on the same plane. Even a slight deviation can generate unwanted forces, altering the dynamic behavior of the FSS.

Therefore a trade-off analysis using as FoMs the complexity, the weight and the cost has been made to estabilish the best configuration.

FoM	Single 100mm air bearing	Single 80mm air bearing	3x 40mm air bearings	3x 25mm air bearings
Weight [lb]	0.97	0.52	0.24	0.09
Cost ($)	587	444	675	636

Table 3.12: Preliminary trade-off analysis of the air bearing configurations with technical data related FoMs

FoM	Complexity	Weight	Cost	Rank
Complexity	1	2	3	**0.455**
Weight	1/2	1	2	**0.318**
Cost	1/3	1/2	1	**0.227**

Table 3.13: Prioritization matrix of FoM for the air bearings trade-off using the AHP Method

	Single 100mm air bearing	Single 80mm air bearing	3x 40mm air bearings	3x 25mm air bearings
Complexity	0.375	0.375	0.125	0.125
Weight	0.467	0.714	0.868	0.951
Cost	0.752	0.813	0.704	0.732
Total Rank	0.489	**0.582**	0.492	0.525

Table 3.14: Decision matrix for the air bearing configurations

As a result of the trade-off analysis the final design opted for a single, larger porous flat rounded air bearing with a diameter of 80 mm by NEWWAY shown in Figure 3.12. The single air bearing configuration reduced the number of components and should simplify both the assembly process and the maintenance of the system during time.
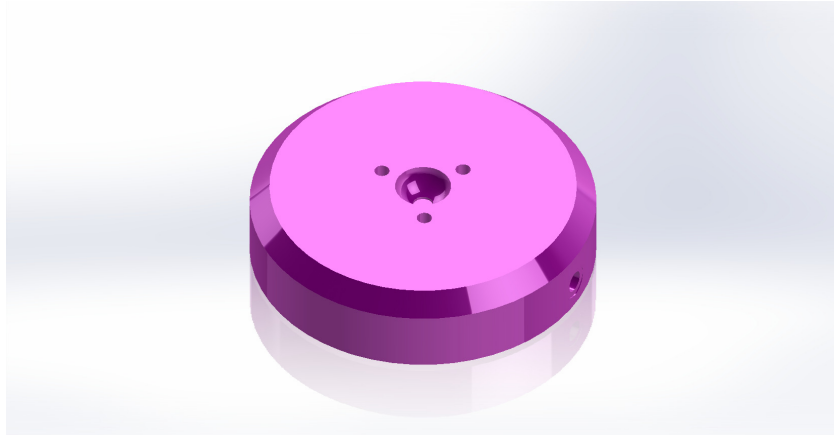
Figure 3.12: CAD of the air bearing

Other key elements of this system include an air tank and solenoid valves equipped to nozzles functioning as gas thrusters, along with connecting components and pressure regulation devices that ensure precise air delivery.

The airflow originates from the air tank, a compact and refillable high-pressure air (HPA) tank chosen to maintain a compact design. Specifically, the FSS uses a HPA System 3000Psi PT Reg 0,4l alloy by Protoyz [60].

Since there are no big differences in air tanks performances, this air tank has been chosen to maximize the internal volume of the structure while guaranteeing small dimensions and high capacity.

The thrust is generated by solenoid valves connected to a custom-built laval nozzle developed by the Spacecraft Robotics Laboratory acting as thrusters [61] already used for the MyDAS and NPS projects. The nozzle has been designed starting from the desired output thrust and is a convergent-divergent nozzle as shown in Figure 3.13

This method has been widely employed in similar applications so it represents a well-documented and reliable solution as seen in Section 2.3. To avoid unnecessary complexity, the propulsion system from [24] has been adopted, consisting of two sub-miniature solenoid valves by GEMS paired with two servo motors and two nozzles. This configuration enables precise thrust vectoring and generates an estimated thrust of 0.1 N at 4.1 bar and 0.16 N at 6.9 bar [62]. From the data presented in Section 2.3, this value aligns with the thrust requirements for a system of the size and weight proposed in this project. In fact, for the application of this propulsion system in [24], it was observed that the system was oversized, requiring smaller rotation angles. In this case, thanks to the higher weight, it will be possible to utilize greater angles.

The decision to use this system was primarily driven by the need to minimize
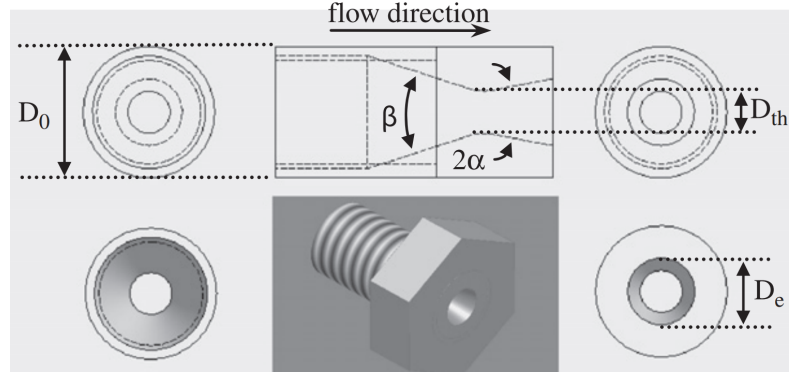
Figure 3.13: convergent-divergent nozzle from SRL [1]

Figure 3.14: The GEMS solenoid valve [63]

prototyping time by utilizing readily available components, thus avoiding the need to order new ones. Once the testbed is installed, potential modifications to this configuration can be explored and evaluated after a preliminary test phase on the granite matching plane.

While the solenoid valves regulate the flow of propellant, servos direct them enabling thrust vectoring.

For the choice of the servo a trade-off approach has been used. Starting from the research of the most common servos used in similar applications [24] other alternatives have been detected based on similar specifics. In Table 3.15 is possible to see the main specifics.

Then, as shown in Table 3.17, it is possible to normalize the value of the FoM in order to reach the final score for each servo.

FoM	SG90	HD-1810MG	MG90S	EMAX ES08MD II
Torque (kg · cm) at 4.8V	1.2	3.6	2.2	2.6
Torque (kg · cm) at 6V	1.6	4.2	2.5	3.0
Speed (sec/60°) at 4.8V	0.12	0.11	0.11	0.12
Speed (sec/60°) at 6V	0.10	0.09	0.10	0.10
Weight (g)	9	16	13.4	14.5
Cost (€)	4	18	6	12

Table 3.15: Preliminary trade-off analysis of the servos with technical data related FoMs

FoM	Torque	Speed	Weight	Cost	Final Rank
Torque	1.00	1.00	4.00	7.00	**0.41**
Speed	1.00	1.00	4.00	7.00	**0.41**
Weight	0.25	0.25	1.00	4.00	**0.14**
Cost	0.14	0.14	0.25	1.00	**0.04**

Table 3.16: Priority matrix for servo parameters with final rank

	SG90	HD-1810MG	MG90S	EMAX
Torque	0.1495	0.3364	0.2336	0.2804
Speed	0.7561	0.7805	0.7561	0.7073
Weight	0.8299	0.6975	0.7467	0.7259
Cost	0.9000	0.5500	0.8500	0.7000
Total Rank	0.5235	**0.5776**	0.5443	0.5346

Table 3.17: Decision matrix for the servo using AHP method

As a result of the trade-off analysis, the best option is the servo HD1810MG.

Figure 3.15: The servo HD 1810MG [2]

In particular a configuration with two vectorable thrusters is used, positioned opposite each other relative to the center of mass. in this way, when the servos are set to their default position at 0°, both thrusters face outward in opposite directions. Firing one of the thrusters results in linear acceleration in the opposite direction. To achieve sideways movement, both servos have to face the same direction in the plane; in contrast, by rotating the servos facing opposite directions enables the ability to rotate the FSS.
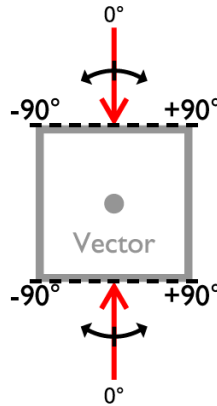
Figure 3.16: Vector congiguration of the servo as thrusters [62]

Finally, to meet the operating pressure requirements of the solenoid valves and air bearing, two pressure regulation step are necessary, one with an high-pressure regulator to lower the pressure from 300 bar to an intermediate level of around 60 bar, and the other with a low-pressure precision regulator to further reduce the pressure to the operating pressure of the solenoid valves. This could be achieved using the already built in regulator of the tank and a Parker high-pressure regulator and a 90° pressure regulator from Palmers Pursuit Shop, capable of handling input pressures up to 310 bar and adjusting the output pressure within a range from 0 to 8.6 bar.

After being adjusted to the correct pressure, the air is distributed to the solenoid valves and air bearing through a network of tubing.

3.5.4   Electrical Power System (EPS)

In Figure 3.5 it is highlighted that the EPS plays a crucial role for the entire FSS providing power to all the subsystems.

First of all it is evident that the system should powered by a portable power bank, which provides a compact, self-contained power source for all onboard electronics and at the same time it doesn't have wires that potentially could interfere with the system.

In addition the power requirements of the FSS components vary, with the OBC requiring 5V and the solenoid valves needing 12V. All the components and their respective operating voltages are reported in Table 3.19 in order to have a clearer overview of the system. To accommodate these differences a single battery can still be used in conjunction with voltage converters. The power bank outputs 19V, which is stepped down to 5V using a dedicated voltage converter.

Given those observations and the power budget reported in Section 3.7 the main characteristics of the battery can be listed in Table 3.18.

Specification	Minimum request
Voltage	5/19 V
Power	45 W
Current	4 A
Dimensions	17,3mm W x 8,1mm H x 2,3mm D

Table 3.18: Requested specifications for the power bank

As stated before, the power distribution has to be splitted and that can be made through a Y-harness, which splits the power output from the battery into two circuits, each designed to meet specific voltage requirements.

In conclusion, for the EPS a power bank with at least 45 W and an output of 5/19 V is needed.

One possible solution has been identified in the the INIU 20000mAh 65W power bank shown in Figure 3.17.

Component	Voltage
Jetson Orin AGX	5V
Solenoid Valves	12 V
Reaction wheel	5 V
Servo Motor	5V
IMU	5V

Table 3.19: Components voltage

Figure 3.17: The INIU power bank [3]

3.5.5 Thermal Control System

The thermal control system (TCS) of the FSS aim to keep all components within their safe operating temperature ranges, as shown in Figure 3.2, thereby ensuring optimal performance and longevity. The system should be designed to handle a variety of external conditions, including fluctuating ambient temperatures and the internal heat generated by high-performance components but in the specific context of laboratory testing, there are no significant temperature variations in the ambient, so most of the elements in this FSS remain well within their standard temperature tolerances, presenting minimal thermal challenges. A notable exception is the NVIDIA Jetson Orin processor, which, as a high-performance computing platform if left unsupervised is subject to overheating. To prevent it, an active cooling solution, such dedicated fan, can be introduced. This fan draws heat away from the processor, enabling it to operate at high loads without sacrificing performance. A key advantage of this FSS design is the external placement of the on-board computer (OBC). By positioning the OBC externally, the heat generated by the processor is effectively isolated, preventing thermal spread to other components.

An Nvidia fan has been chosen in order to ensure full compatibility with the OBC, guaranteeing an easy integration within the system as shown in Figure 3.18.

Figure 3.18: The NVIDIA fan, credit:NVIDIA

3.5.6 Communication System

Starting Figure 3.2 it is clear that a Wi-Fi-based Communication System can be utilized to establish a reliable, high-speed connection between the onboard module and the dedicated laboratory workstation. Wi-Fi was chosen over other wireless communication technologies, such as bluetooth, due to its higher data transfer rates, longer range, stable connectivity, and power efficiency [64].

Differents Wi-Fi boards have been considered as shown in Table 3.20.

Board	Wi-Fi	Bluetooth	Transmitted Power (dBm)	RAM (KB)	Cost (€)
ESP32	Yes (2.4 GHz)	Sì (BLE 4.2/5.0)	19.5	520	9
ESP8266	Yes (2.4 GHz)	No	17	160	5
TI CC3200	Yes (2.4 GHz)	No	18	256	62
SAMW25	Yes (2.4 GHz)	No	18	256	65

Table 3.20: Comparison between the Wi-Fi boards

Since the differences between these boards are minimal, the AHP method may not be particularly meaningful in this case. Given the small performance gap, a direct comparison of key specifications may be sufficient to support the decision-making process without requiring a structured multi-criteria evaluation.

In this specific case, the decision was made to opt for the ESP32, as it offers a balance of performance, relative low power consumption, and integrated Bluetooth Low Energy (BLE) connectivity. While BLE is not essential for the current configuration of the FSS, its presence ensures greater flexibility for potential future modifications to the FSS, expanding communication options as needed.

The core of the communication system is the ESP32 module, selected for its compact size, energy efficiency, and ease of integration. This module is a self-contained system-on-chip (SoC) with an integrated TCP/IP protocol stack, enabling independent Wi-Fi connectivity while also providing BLE support for extended wireless communication capabilities.

Operating at a voltage of 3.3V, supplied by a voltage regulator within the system, the ESP32 features a self-calibrated RF circuit, allowing it to function effectively without the need for additional external components.
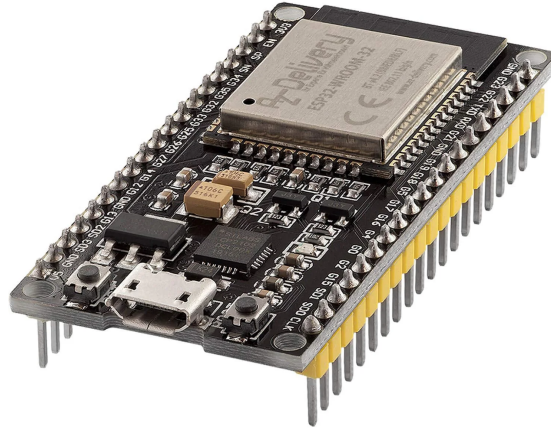
Figure 3.19: The ESP32 communication module [4]

3.5.7   Attitude Determination and Control System

The ADCS is a critical subsystem for this application since has to be designed to
determine and control the orientation of a device, often in response to mission-
specific requirements as shown in Figure 3.2. The ADCS function involves collecting
and processing data from various sensors to calculate the device's orientation and
motion data in order to use these information to apply the necessary corrections to
maintain or change the attitude as needed.

The primary sensor used for the system is an Inertial Measurement Unit (IMU),
which combines an accelerometer and a gyroscope to provide essential data on
motion and orientation. The accelerometer measures linear acceleration along three
axes, allowing the detection of changes in velocity and the identification of external
forces. The gyroscope, meanwhile, measures angular rates of rotation around the
same axes. By integrating the data from both sensors over time, the system can
estimate position, velocity, and attitude with high accuracy.

Selecting an IMU that can take full advantage of the OBC capabilities is crucial.
The Jetson Orin's advanced I/O and processing capacity allows it to handle higher
data rates and execute more complex sensor fusion algorithms, making it ideal for
real-time robotics and control systems.

A suitable IMU would be the Bosch BNO055 [65]. This could be the preferred
choice over the others, as it delivers similar performance at a lower cost while
integrating onboard sensor fusion, making it ideal for applications requiring ef-
ficiency and ease of use. The BNO055, shown in Figure 3.20 is a smart sensor

IMU	DOF	Sensor Fusion	Interfaces	Power (mW)	Module Size (mm)	Cost (€)
Bosch BNO055	9	**Yes** (Integrated)	I²C, UART	39.6	$20 \times 15 \times 3$	11
ICM-20948	9	No (External Processing)	I²C, SPI	16.5	$14 \times 10 \times 2$	37
LSM9DS1	9	No (External Processing)	I²C, SPI	19.8	$14 \times 10 \times 2$	24
Xsens MTi-3	9	**Yes** (Advanced)	UART, SPI	165	$12 \times 12 \times 2.5$	331

Table 3.21: Comparison of IMUs Specifications

integrating a 3-axis accelerometer, gyroscope, and magnetometer with an onboard sensor fusion processor, providing highly accurate orientation data with minimal processing required from the host device. It supports I2C and UART communication protocol, compatible with the OBC's GPIO pins, and outputs position, velocity, and orientation directly, reducing the Orin's computational load.

To integrate one of these IMUs with the Jetson Orin, the sensor can connect via the I2C or UART interface on the Orin's GPIO pins. Using libraries such as Jetson.GPIO for Python, seamless communication between the IMU and the Jetson platform can be achieved.
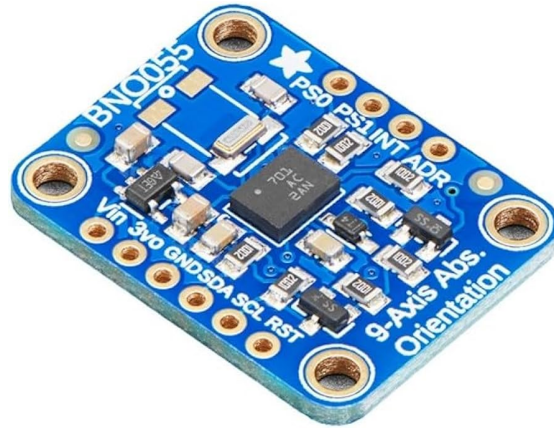
Figure 3.20: Bosch BNO055 IMU [5]

In order to provide error detection and correction for data transmission it is possible to combine the IMU with an external tracker. The most convenient solution could be to adopt a VICON tracker, that can track the position of the FSS using passive markers applied on its surface and then transmit the acquired data via WI-Fi. Once obtained the position data, is it possible to obtain speed and acceleration value by deriving them.

Reaction Wheel

Precise control over rotational movements requires dedicated actuation mechanisms. For the FSS, a single reaction wheel is necessary to manage rotation since it is costrained to only one rotational DoF.

The reaction wheel operates by leveraging the principle of conservation of angular momentum: as the wheel accelerates or decelerates, the FSS experiences a counter-rotation in the opposite direction. Since the FSS can be seen as a small cubesat in Table 3.22 is possible to see some possible options based on common reaction wheels used in similar applications with their relative technical data.

	Rocket Lab RW-0.003	**CubeWheel CW00500**	**AAC Clyde Space RW222**
Maximum angular momentum	3 mNms	50 mNms	6 mNms
Maximum torque	±1 mNm	10 mNm	±2 mNm
Maximum speed	8.500 rpm	10.000 rpm	15.000 rpm
Dimensions (mm)	33,5 x 33,5 x 17	67 x 25 x 46	25 x 25 x 15
Weight	<50 g	400 g	N/A
Power consumption	4,5 - 9 V	12 V	3,3 V
Interface	UART o I²C/SMBus	CAN/UART/RS-485	I²C
Operative temperature	-40°C to +70°C	-20°C to +80°C	-20°C to +60°C

Table 3.22: Comparison between commonly used reaction wheels for small cubesats

In this case the trade-off analysis must be approached in a more qualitative manner, as certain data are either unavailable or imprecise in the technical datasheets, which may lead to potential distortion of the results.

The CubeWheel CW005000 demonstrates better performance, but the performance difference compared to the other two options is not significant enough to justify its notably higher weight. While the AAC Clyde Space RW222 presents an appealing solution, the absence of precise weight data ultimately led to the decision to select the Rocket Lab RW-0.003.

The selection of the Rocket Lab RW-0.003 is primarily driven by the need to position the wheel inside the structure on a planar surface, making size reduction a crucial factor. Furthermore, its compact design contributes to minimizing the overall system weight, which aligns with the project guidelines outlined Section 3.4. Since the tests will take place in a laboratory environment, top performance is not a priority, enabling the adoption of a lighter and more compact solution. Thus, the Rocket Lab RW-0.003 emerges as the optimal balance between compactness, reduced weight and adequate performance for the experimental phase.

Another solution that can be implemented is to design a RW *ex-novo* using a generic electric motor with a flying wheel attached to it since it can provide the same kind of performances while drastically reducing the cost since for ground
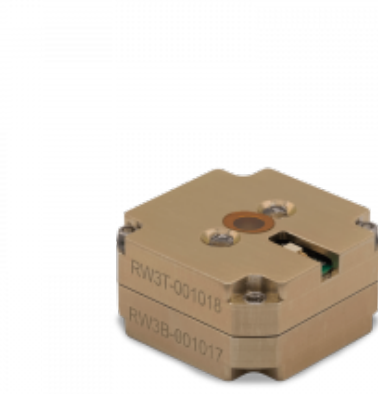
Figure 3.21: Rocketlab 3mNm reaction wheel [6]

testing space-qualified components are not strictly necessary. However, for this preliminary phase, it is preferable to prioritize tested off-the-shelf components.

As a preliminary design the Rocketlab 3mNm reaction wheel is choosen.

3.6 Preliminary design of the FSS

Finally, in Figure 3.23 the preliminary assembly is presented, including its main components, while excluding the pneumatic tubes for simplicity. As previously mentioned, one of the key aspects of this project is modularity. Specifically, all modules are designed with the same attachment interface to the structure, allowing them to be easily swapped or replaced even if some specific requirements of the system will be changed.
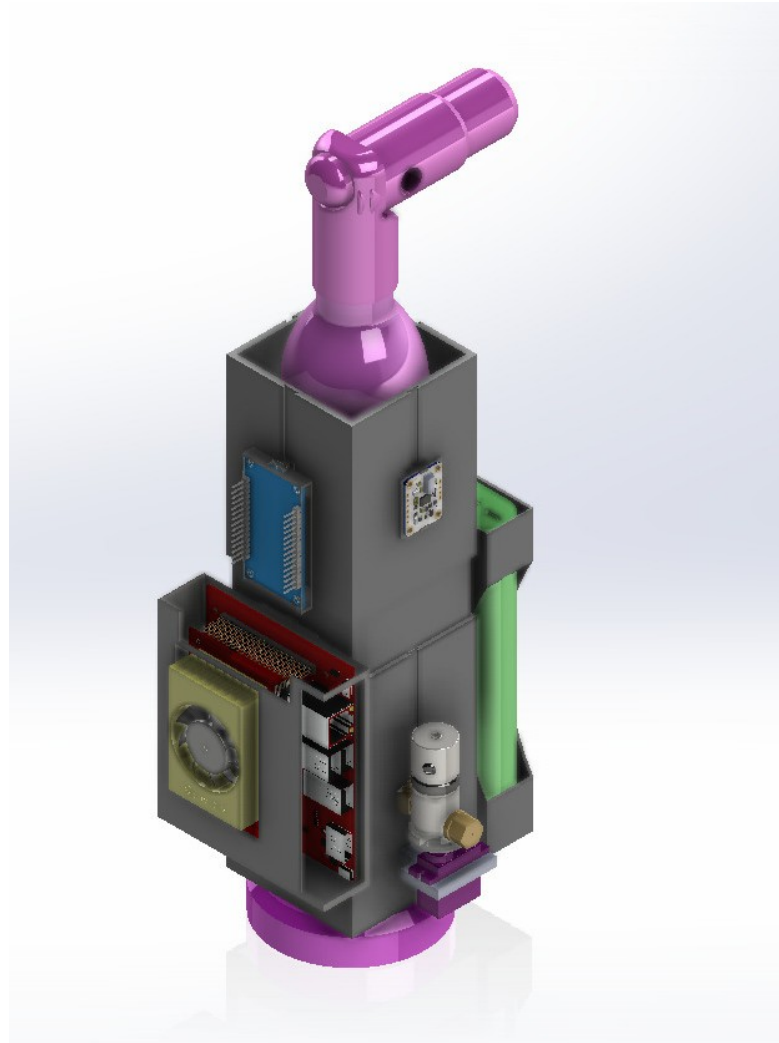
Figure 3.22: CAD Assembly

Figure 3.23: CAD Assembly

3.7   Preliminary Power Budget

From Figure 3.4, it is possible to create a preliminary power budget by considering the most demanding scenario in terms of power requirements, which has been used for sizing the battery. In this case, the mode that demands the most energy is the operation mode. Therefore, we can derive the preliminary power budget by considering the requested power of each active component in the operative mode, as shown in Table 3.23.

Component	OBC	Solenoid Valves	IMU	Servo motors	RW	Wi-Fi board	Total
Power [W]	40	1,3	0,0396	2,88	0,03	0.078	44,32

Table 3.23: Preliminary Power Budget of the FSS

57

3.8   Preliminary Mass Budget

Lastly, it is possible to define a mass budget by accounting for all the components discussed in the previous sections. At this stage of the project, the weight of the tubing have been excluded from the evaluation, as its consideration would not be relevant or meaningful in the current phase of development. Furthermore, for the reaction wheel, the maximum possible value has been selected due to the lack of precise information available in the datasheet.

Component	Mass[gr]
NVIDIA jetson Orin 32GB	280
Air tank	925
Air bearing	240
Power bank	490
Servo	32
Solenoids valves equipped to nozzles	154
Structure	302
Pressure regulator	260
IMU	5
Wi-Fi board	5
Fan	30
Reaction Wheel	50
Total	**2774**

Table 3.24: Preliminary mass budget of the FSS

Chapter 4

Logistic and installation of the granite matching plane

In this thesis work, granite was selected first of all to maximize surface refinement but mostly due to the use of granite for similar applications as seen in Figure 2.9. Maximizing the dimensions of the granite plane remained a priority in order to have a larger testing area, but this required a trade-off with the limitations of the laboratory's size and the cost of the granite plane.

The laboratory designated for the installation of the granite plane spans approximately 12.6 m × 6.6 m and currently houses workbenches and a station for 3D printing. It was essential not only to allocate sufficient room for the granite testbed but also to leave enough space to provide a sufficiently large operational area for conducting experiments and allowing free movement for personnel. Consequently, the dimensions of the granite plane were carefully chosen to balance the need for an adequately sized testing surface while ensuring the laboratory retained the necessary flexibility and accessibility to support experimental activities and workflow efficiency.

So after a preliminary evaluation of all these factors a granite plane measuring 3.5 x 4 meters was selected, with a total weight of approximately 27 tons as it's possible to see in fig. 4.1. The estimated weight was obtained from the CAD model, shown in Figure 4.1, by multiplying the volume by the average density of granite, which is 2.69 g/cm^3.

The significant weight of the granite plane, resulting from the material's inherent density and rigidity, plays a crucial role in enhancing its stability. This substantial mass effectively minimizes unwanted vibrations and movements during experimental operations, thereby contributing to the overall integrity and reliability of the experimental results.

Figure 4.1: Granite matching plane draw

The granite floor is supported by three sturdy supports: one central support, larger in size to ensure uniform weight distribution and optimal structural stability, and two lateral supports that help balance the load and prevent bending or distortion of the surface. This support configuration is crucial for maintaining the flatness of the floor during use, especially when variable forces or loads are applied to different points on the surface.

4.1 Logistics, installation and setup of the testbed

The testbed set up for the project involves the use of the granite matching plane in Figure 4.1. One of the initial activities carried out was logistic planning for integrating the testbed within the laboratory taken in consideration. The logistic plan focuses mainly on the most effective position of the granite floor within the available laboratory space, taking into account both operational needs and safety requirements. The placement of supports for the granite floor in the test bed of the FSS is crucial for ensuring structural integrity and accurate performance testing. In addition, proper support placement determines where geological probing should occur, allowing for a robust foundation that can sustain the simulator's weight and operational stresses.

To start, the laboratory floor planimetry was analyzed in detail identifying locations to avoid. A conservative approach was adopted to ensure that even areas that would otherwise be borderline without the additional margins could potentially become viable for optimal positioning within the laboratory. This was achieved while maintaining a uniform and streamlined arrangement by avoiding the use of half-tiles along the edges of certain sides of the laboratory. This decision

was carefully made to meet the requirements for movement around the testbed, reducing potential complexities in both the planning and implementation phases.

The first challenge presented by the structural constraints was the presence of a floating floor in the laboratory. A floating floor is a type of flooring installation where the tiles are not directly attached to the sub-floor. As a result, the supports could not be placed on the floating floor itself and had to be positioned directly on the sub-floor. So all the tiles where removed in order to have a clear view of the sub-floor. In Figure 4.2 an initial layout of the laboratory is presented. Each square in the grid represents a tile of the floating floor, which serves as reference for the subfloor alignment once the tiles are reinstalled, therefore each square in the schematization represents a square tile with a side length of 60 cm in reality. In addition, the electrical panel has been highlighted in yellow and the doors in black. It is evident that the side of the laboratory containing the door and the electrical panel cannot accommodate the granite plane supports in two rows. This restriction arises from the presence of metal structures housing electrical cabling, which make those areas unsuitable for support placement.

Additional critical areas that cannot be utilized are the sixth row of tiles and the first column, which contains metal structures housing electrical cabling. These installations further limit the possible placement of supports for the granite plane, as they obstruct the subfloor in this section.

First, all these areas were excluded. Specifically, the area surrounding the electrical panel was considered unsuitable for floor placement because it is necessary to ensure sufficient clear space for operators access in case of maintenance or emergencies.

In addition to these areas to avoid, it must also be considered that along the edge of the tiles there are steel partitions on which the floating floor is based. Therefore, the supports cannot rest at the interface between one tile and another, but only in the central area of the tile.

Another soft requirement was the preference to place the workbench on the left side of the laboratory, as there are tables and workstations along the x-axis in Figure 4.2, starting from the middle of the room, which should ideally not be moved.
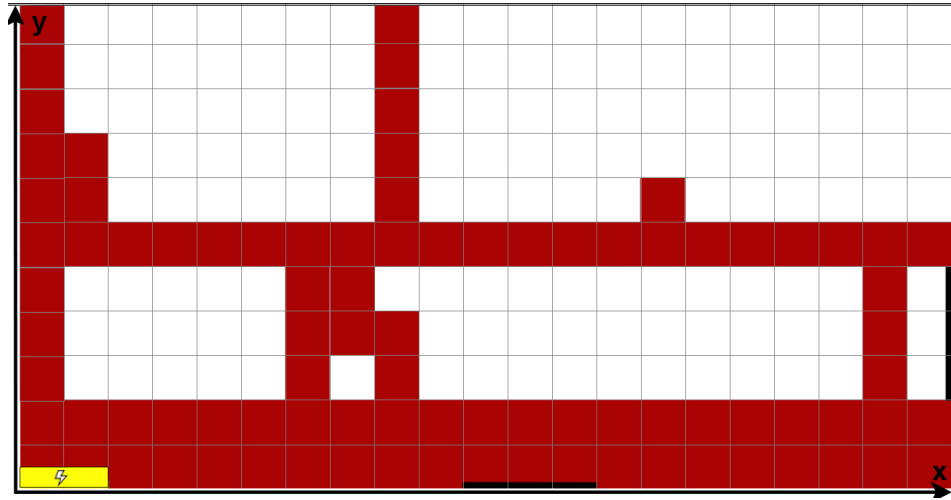
Figure 4.2: Schematization of the ASTRADORS's laboratory

After identifying the areas to avoid, the usable space for positioning the granite floor was determined by exclusion. Within this area, the most efficient layouts were chosen based on several secondary requirements. These included ensuring sufficient access space of at least 60 cm between the floor and the surrounding walls to allow operator movement, facilitate repairs, and prevent the simulator from becoming stuck. The area near the electrical panel was kept clear to ensure unimpeded access for maintenance or emergencies. Moreover, the granite floor was positioned at least 120 cm away from doors to maintain clear passage and avoid obstructing access to the room.

Taking these constraints into account, two potential configurations for positioning the floor were evaluated: one with its longer side parallel to the X-axis Figure 4.4 and the other with its longer side perpendicular Figure 4.3.

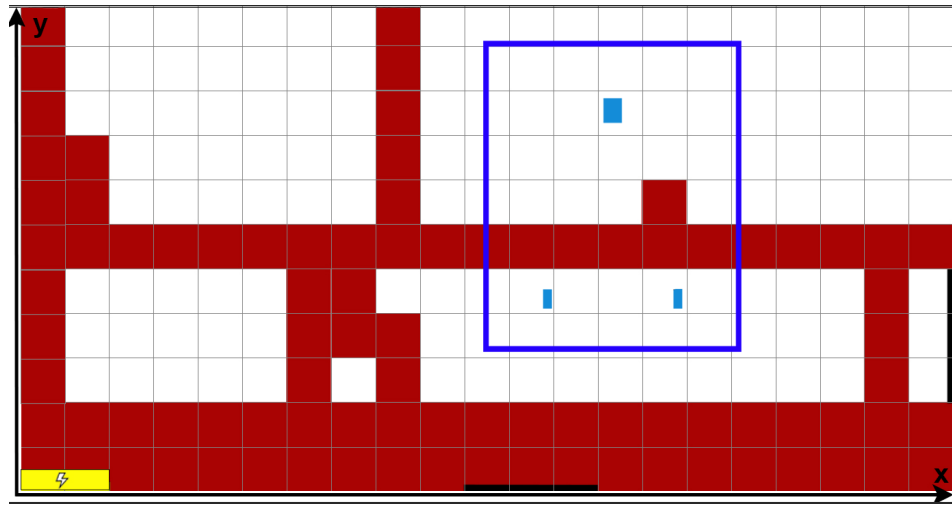**Figure 4.3:** Possible configuration for the granite floor with the longer side perpendicular to the X axis
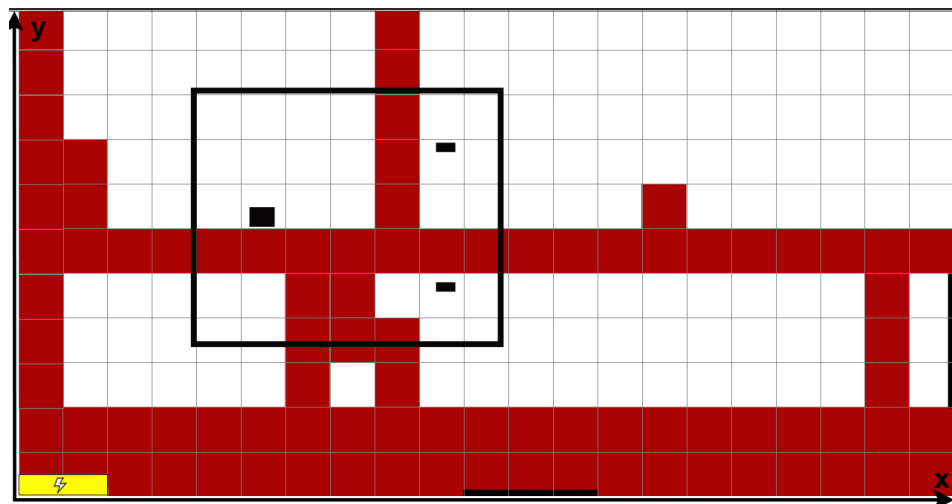

Figure 4.4: Possible configuration for the granite floor with the longer side parallel to the X axis

So, in conclusion, the logistics part concerning the position of the granite floor in the laboratory ends with the provisional selection of the described possible configurations.

4.2 Granite floor transport and installation

Transporting and installing a heavy weight granite floor inside a laboratory is a challenging task that requires meticulous planning, specialized equipment and a coordinated team effort. The process involves several stages, from selecting the appropriate transport machinery to removing structural barriers for insertion, ensuring that every step is executed with precision to avoid damage to the granite plane or the laboratory infrastructure.

4.2.1 Transportation to the Laboratory Site

The first issue to be tackled in the installation process is transporting the granite plane from its manufacturing location to the laboratory site. Given the floor's weight of around 27 tons, a specialized heavy transport vehicle is essential. Depending on the specific needs and circumstances, several types of trailers can be used, including low-bed trailers, multi-axle hydraulic modular trailers (HMTs), and electric-assisted heavy transport trailers. These vehicles are designed to carry extremely heavy and oversized loads, ensuring stability and safety during transport:

- **Hydraulic Modular Trailer**: this highly versatile and robust solution is ideal for transporting heavy granite slabs, offering exceptional load-bearing capacity and stability. Its hydraulic axle system ensures even weight distribution, minimizing strain on the trailer and reducing the risk of damage to the load. The modular design enhances flexibility, allowing customization to match the slab's dimensions and weight. In addition to this, the low-bed configuration lowers the center of gravity, improving stability and safety during transit. These features, combined with superior maneuverability for navigating tight or complex routes, make hydraulic modular trailers the optimal choice for oversized and heavy cargo.

Figure 4.5: Example of a low bed design [66]

- **Electric-Assisted Heavy Transport Trailer**: an electric-assisted trailer offers an innovative solution by integrating electric motors into a traditional towing system, providing additional power to support the towing vehicle. Unlike fully electric trailers, it does not rely solely on battery power, combining the strengths of electric assistance with the reliability of conventional towing. This system enhances overall transport efficiency, reduces fuel consumption, and improves maneuverability, especially in challenging conditions. On the other side they are generally designed to support lighter heavy loads.

Figure 4.6: Example of an electric trailer solution:the ADDRIVE by Goldhofer [67]

- **Fully Electric Trailer**: for projects focused on sustainability, a fully electric heavy transport trailer offers a highly eco-friendly solution. Equipped with its own electric motors and batteries, this trailer provides a quiet, emission-free option for transporting massive loads. Furthermore, it operates at significantly lower noise levels compared to diesel-powered alternatives, which is especially beneficial in urban areas with noise restrictions. The fully electric trailer also enhances energy efficiency, particularly over shorter distances, and often features regenerative braking technology to optimize energy use. However, despite these advantages, fully electric trailers typically have limited load capacities compared to traditional or hydraulic trailers. While suitable for transporting heavy loads, they are generally designed for moderately heavy cargo, and transporting a 27-ton granite plane could require specialized, high-capacity models, which are still less common and more costly.

In Table 4.1 are resumed the main advantages for each type:

	Hydraulic	**Electric-assisted**	**Fully electric**
Main Advantages	Low center of gravity Higher load capacity	Energy efficiency Maneuverability	Zero emissions Reduced noise levels

Table 4.1: Main advantages of the transportation types

65

The choice of a hydraulic system for this case is primarily driven by its higher load capacity and greater operational range, making it the most suitable solution for handling heavy loads and ensuring extended mileage.

4.2.2   Unload of the Granite Matching Plane

Once the granite plane arrives at the laboratory site, it will be unloaded using one or two electric cranes. These cranes will utilize holes located along the sides of the granite plane, into which pins can be inserted to safely lift the heavy granite plane . The electric cranes will then transport the granite plane into the laboratory. However, due to the dimensions of the laboratory doors not being large enough to accommodate the granite plane, it will be necessary to demolish one of the drywall walls to create a passage for the cranes. After the wall is removed, the cranes will carefully position the granite plane inside the laboratory, ensuring it is placed in the desired location.

To ensure the granite plane is handled properly, the cranes must have a lifting capacity of at least 27 tons. Additionally, they must be compact and lightweight to allow for smooth navigation within the confined space of the laboratory. Potential crane models that meet these criteria include the 55/60iE crane by Ormig and the mc300s crane by NMG.
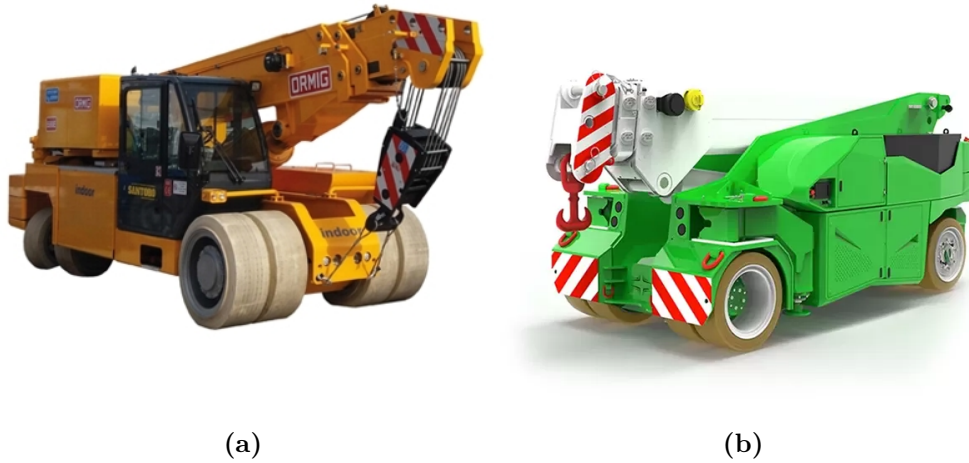

(a)   (b)

Figure 4.7: Crane Models: (a) Ormig 55/60iE [68] and (b) NMG MC300s [69]

Finally the installation plan led to the conclusion that the optimal configuration for this thesis's needs involves transportation via hydraulic trailer, supported by electric cranes. Moreover, given the dimensions of the building's entrance, which is approximately 3.65 meters, the most efficient solution was identified as shown in Figure 4.4. This configuration allows for the direct installation of the granite plane without the need for additional maneuvering inside the laboratory, thus reducing the risk of damage and avoiding unnecessary complexities. In particular, keeping in mind that each square measures 60 cm and represents a tile, the ideal position, following the previous logistical considerations, is given by P0 in (330, 380), P1 in (574, 282), and P3 in (574, 478).

Chapter 5

Conclusions

In conclusion, this thesis provides a comprehensive overview of the state of the art for reduced gravity simulators, offering insights into the existing technologies.

The study focused on modelling the system using the Systems Engineering approach, with tools such as the functional diagram, the N2 diagram and the functions/products diagram to define the preliminary design of the Floating Spacecraft Simulator. The application of the SE approach guarantees that the final structure design is flexible, scalable and easily replicable, enabling future expansions or modifications.

The analysis of the system requirements enabled the preliminary identification of the necessary components, with a particular emphasis on the guidelines of the preliminary design of the floating spacecraft simulator.

A detailed logistical plan was developed to determine the optimal placement of the granite matching plane within the laboratory at the Politecnico di Torino.

The installation plan of the granite matching plane led to the conclusion that the most suitable solution for the transport of the granite plane is via a hydraulic trailer due to their higher load capacity, then for the positioning in the laboratory an high capacity electric crane is used to minimize noise and emissions. Moreover the most final position in the laboratory for the granite plane was identified in Figure 4.4. This configuration is optimal both in terms of ease of installation and compliance with the identified logistical requirements.

5.1   Future improvements

Several upgrades can be introduced both in the floating spacecraft simulator and in the matching plane to achieve improvements.

First and foremost, since software integration is not part of the preliminary design phase but a subsequent step, it is important to conduct a more detailed

analysis to identify the most effective AI solutions to implement by researching and studying the use of these technologies in similar applications. While neural networks and reinforcement learning are among the most promising approaches, it would also be worth exploring convolutional neural networks (CNNs) and deep learning (DL) to determine the most suitable AI technology based on the specific types of maneuvers being analyzed.

For instance, CNNs could be applied to trajectory mapping or obstacle avoidance, while neural networks and reinforcement learning could be used to conduct extensive trial tests. This would allow the system to train itself and eventually predict the best strategy for each maneuver based on the provided inputs.

At a more advanced stage, further modifications to the internal sensor system could be considered to optimize propulsion performance through AI-driven improvements.

Obviously the implementation of these improvements with more sensors will not be a problem in terms of integration thanks to the modular approach used for the preliminary design of the floating spacecraft simulator.

Another future upgrade could be testing the interaction between more floating spacecraft simulators to simulate maneuvers between a target and a chaser.

Finally, a feasibility study should be conducted on the actuation system for the granite matching plane, which could potentially eliminate the need for a propulsion system internal to the floating spacecraft simulator, but since this would involve a 27-ton structure, a careful planning is required to address the significant power demands involved.

Bibliography

[1]   Claudio Lugini and Marcello Romano. «A ballistic-pendulum test stand to characterize small cold-gas thruster nozzles». In: *Acta Astronautica* 64.5-6 (2009), pp. 615–625 (cit. on pp. vii, 45).

[2]   HobbyKing. *Power HD 1810MG Metal Gear Coreless Digital Servo*. 2025. URL: https://hobbyking.com/it_it/power-hd-1810mg-metal-gear-coreless-digital-servo-3-9kg-13sec-16g.html (cit. on pp. vii, 47).

[3]   INIU. *INIU Powerbank Caricatore Portatile Compatibile*. 2024. URL: https://www.amazon.it/dp/B0CB1DF4JQ (cit. on pp. vii, 49).

[4]   AZ-Delivery. *ESP32 Development Board*. 2025. URL: https://www.az-delivery.de/it/products/esp32-developmentboard (cit. on pp. viii, 52).

[5]   Bosch Sensortec. *BNO055 Intelligent 9-Axis Absolute Orientation Sensor*. 2016. URL: https://cdn-shop.adafruit.com/datasheets/BST_BNO055_DS000_12.pdf (cit. on pp. viii, 53).

[6]   Rocket Lab. *RW-0.003 Data Sheet*. 2024. URL: https://www.rocketlabusa.com/assets/Uploads/RW-0.003-Datasheet-v3.0.pdf (cit. on pp. viii, 55).

[7]   Eugenio Brusa, Ambra Calà, Davide Ferretto, et al. *Systems engineering and its application to industrial product development*. Springer, 2018 (cit. on pp. 1, 24).

[8]   Tomasz Rybus and Karol Seweryn. «Planar air-bearing microgravity simulators: Review of applications, existing solutions and design parameters». In: *Acta Astronautica* 120 (2016), pp. 239–259. ISSN: 0094-5765. DOI: https://doi.org/10.1016/j.actaastro.2015.12.018. URL: https://www.sciencedirect.com/science/article/pii/S0094576515004634 (cit. on pp. 3, 4, 7, 14, 15, 17, 42).

[9]   European Space Agency (ESA). *Airbus A310 Zero-G*. 2024. URL: https://www.esa.int/Science_Exploration/Human_and_Robotic_Exploration/Research/Airbus_A310_Zero-G (cit. on p. 4).

[10]   Matteo Duzzi. «Spacecraft Rendezvous and Docking Using Electromagnetic Interactions — hdl.handle.net». In: () (cit. on pp. 5, 21).

[11] European Space Agency. *Fly Your Thesis!* 2024. URL: https://www.esa.int/Education/Fly_Your_Thesis (cit. on p. 7).

[12] F. R. Celestino, F. Piergentili, D. Izzo, and L. Summerer. «SatLeash - Parabolic flight validation of tethered-tugs dynamics and control for reliable space transportation applications». In: *ResearchGate* (2017). URL: https://www.researchgate.net/publication/314285521_SatLeash_-_Parabolic_flight_validation_of_tethered-tugs_dynamics_and_control_for_reliable_space_transportation_applications (cit. on p. 7).

[13] European Space Agency (ESA). *Science with out gravity - drop towers.* Accessed: 2024-11-26. 2019. URL: https://www.esa.int/ESA_Multimedia/Images/2019/02/Science_with_out_gravity_drop_towers (cit. on p. 8).

[14] Arjun Bindu Jyothikumar et al. «Experiments in Reduced Gravity Space Environment Using 11 Second Drop Tower and Challenges Involved». In: *Proceedings of the NPC2015 Conference.* India, 2015. URL: https://www.researchgate.net/publication/275099726_NPC2015-Paper_No_16_EXPERIMENTS_IN_REDUCED_GRAVITY_SPACE_ENVIRONMENT_USING_11_SECOND_DROP_TOWER_AND_CHALLENGES_INVOLVED (cit. on pp. 9, 10).

[15] Yuji Kan. «Microgravity combustion experiment using high altitude balloon.» In: *40th COSPAR Scientific Assembly* 40 (2014), PSB–1 (cit. on p. 9).

[16] David Urban. «Drop tower workshop». In: *Annual Meeting of the American Society for Gravitational and Space Research.* GRC-E-DAA-TN11765. 2013 (cit. on pp. 10, 22).

[17] Andrea Sondag and Hansjörg Dittus. «Electrostatic Positioning System for a free fall test at drop tower Bremen and an overview of tests for the Weak Equivalence Principle in past, present and future». In: *Advances in Space Research* 58.4 (2016), pp. 644–677 (cit. on p. 10).

[18] Markus Wilde, Casey Clark, and Marcello Romano. «Historical survey of kinematic and dynamic spacecraft simulators for laboratory experimentation of on-orbit proximity maneuvers». In: *Progress in Aerospace Sciences* 110 (2019), p. 100552 (cit. on pp. 10, 11, 14).

[19] S Kwok-Choon, K Buchala, B Blackwell, S Lopresti, M Wilde, and T Go. «Design, fabrication, and preliminary testing of air-bearing test vehicles for the study of autonomous satellite maneuvers». In: *Proceedings of the 31st Florida Conference on Recent Advances in Robotics, Orlando, FL, USA.* 2018, pp. 10–11 (cit. on p. 12).

[20] Giovanni Palmerini, Marco Sabatini, and Paolo Gasbarri. «Analysis and tests of visual based techniques for orbital rendezvous operations». In: *2013 IEEE Aerospace Conference.* IEEE. 2013, pp. 1–14 (cit. on p. 12).

[21] Marco Sabatini, Giovanni B Palmerini, and Paolo Gasbarri. «A testbed for visual based navigation and control during space rendezvous operations». In: *Acta Astronautica* 117 (2015), pp. 184–196 (cit. on p. 12).

[22] Josep Virgili-Llop, DV Drew, Marcello Romano, GV Hobson, BE Wakefield, and WB Roberts. «Spacecraft robotics toolkit: an open-source simulator for spacecraft robotic arm dynamic modeling and control». In: *6th International Conference on Astrodynamics Tools and Techniques*. 2016 (cit. on p. 12).

[23] Richard Zappulla, Josep Virgili Llop, Hyeongjun Park, Costantinos Zagaris, and Marcello Romano. «Floating spacecraft simulator test bed for the experimental testing of autonomous guidance, navigation, & control of spacecraft proximity maneuvers and operations». In: *AIAA/AAS Astrodynamics Specialist Conference*. 2016, p. 5268 (cit. on pp. 13, 14).

[24] Francesco Bologna. «Design, integration and testing of a small floating spacecraft simulator». PhD thesis. Politecnico di Torino, 2023 (cit. on pp. 14, 17, 44, 45).

[25] Tom Geiss. *Flatness*. Accessed: 2025-03-05. 2014. URL: https://www.gd andtbasics.com/flatness/#:~:text=The%20flatness%20tolerance% 20references%20two,dimensional%20tolerance%20associated%20with% 20it (cit. on p. 15).

[26] Bocchi S.R.L. *Graniitlaud Surface Plate Specifications*. https://www.metric. ee/files/filemanager/files/Bocchi/Graniitlaud.pdf. Accessed: 2024-11-30. n.d. (Cit. on p. 16).

[27] Kazuya Yoshida and Yoji Umetani. «Control of space free-flying robot». In: *29th IEEE Conference on Decision and Control*. IEEE. 1990, pp. 97–102 (cit. on p. 17).

[28] AG Ledebuhr et al. «Micro-satellite ground test vehicle for proximity and docking operations development». In: *2001 IEEE Aerospace Conference Proceedings (Cat. No. 01TH8542)*. Vol. 5. IEEE. 2001, pp. 2493–2504 (cit. on p. 17).

[29] Giovanni Mimmi, C Rottenbacher, Lucia Frosini, Andrea Negri, et al. «An experimental test-bed for microgravity simulation in robotic arm dynamics». In: *Proceedings of 6th International Conference on Dynamics and Control of Systems and Structures in Space, Riomaggiore, Italy*. 2004 (cit. on p. 17).

[30] XH Gao et al. «Development of the Chinese intelligent space robotic system». In: *2006 IEEE/RSJ International Conference on Intelligent Robots and Systems*. IEEE. 2006, pp. 994–1001 (cit. on p. 17).

[31] Ou Ma and George Yang. «Validation of a satellite docking simulator using the SOSS experimental testbed». In: *2006 IEEE/RSJ International Conference on Intelligent Robots and Systems*. IEEE. 2006, pp. 4115–4120 (cit. on p. 17).

[32] Matthew D Lichter, Hiroshi Ueno, and Steven Dubowsky. «Vibration estimation of flexible space structures using range imaging sensors». In: *The International Journal of Robotics Research* 25.10 (2006), pp. 1001–1012 (cit. on p. 17).

[33] Peggy Boning, Masahiro Ono, Tatsuro Nohara, and Steven Dubowsky. «An experimental study of the control of space robot teams assembling large flexible space structures». In: *Proc. of the 9th International Symposium on Artificial Intelligence, Robotics and Automation in Space, i-SAIRAS*. Citeseer. 2008 (cit. on p. 17).

[34] Evangelos Papadopoulos, Iosif S Paraskevas, Thaleia Flessa, Kostas Nanos, Georgios Rekleitis, and Ioannis Kontolatis. «The ntua space robot simulator: Design & results». In: *ESA Workshop on Advanced Space Technologies for Robotics and Automation (ASTRA 2008)*. Citeseer. 2008 (cit. on p. 17).

[35] Daniel P Scharf, Jason A Keim, and Fred Y Hadaegh. «Ground demonstration of synchronized formation rotations for precision, multi-spacecraft interferometers». In: *3rd International Symposium on Formation Flying*. 2008 (cit. on p. 17).

[36] Dae-Min Cho, Dongwon Jung, and Panagiotis Tsiotras. «A 5-dof experimental platform for spacecraft rendezvous and docking». In: *AIAA Infotech@ Aerospace Conference and AIAA Unmanned… Unlimited Conference*. 2009, p. 1869 (cit. on p. 17).

[37] Naohiro Uyama, Håvard Lund, Koki Asakimori, Yuki Ikeda, Daichi Hirano, Hiroki Nakanishi, and Kazuya Yoshida. «Integrated experimental environment for orbital robotic systems, using ground-based and free-floating manipulators». In: *2010 IEEE/SICE International Symposium on System Integration*. IEEE. 2010, pp. 108–113 (cit. on p. 17).

[38] Jason S Hall, Marcello Romano, A Milella, D Di Paola, and G Cicirelli. *Laboratory experimentation of guidance and control of spacecraft during on-orbit proximity maneuvers*. INTECH Open Access Publisher, 2010 (cit. on p. 17).

[39] Markus Schlotterer and Stephan Theil. «Testbed for on-orbit servicing and formation flying dynamics emulation». In: *AIAA Modeling and Simulation Technologies Conference*. 2010, p. 8108 (cit. on p. 17).

73

[40] Tomasz Rybus et al. «New planar air-bearing microgravity simulator for verification of space robotics numerical simulations and control algorithms». In: *12th ESA Symposium on Advanced Space Technologies in Robotics and Automation*. Vol. 8. 2013 (cit. on p. 17).

[41] Kelsey Saulnier, David Perez, Grace Tilton, Daniele Gallardo, Chris Shake, R Huang, and Riccardo Bevilacqua. «Operational capabilities of a six degrees of freedom spacecraft simulator». In: *AIAA Guidance, navigation, and control (GNC) conference*. 2013, p. 5253 (cit. on p. 17).

[42] Josep Virgili-Llop, Costantinos Zagaris, Hyeongjun Park, Richard Zappulla, and Marcello Romano. «Experimental evaluation of model predictive control and inverse dynamics control for spacecraft proximity and docking maneuvers». In: *CEAS Space Journal* 10 (2018), pp. 37–49 (cit. on pp. 17, 25).

[43] Ayansola D Ogundele, Bautista R Fernandez, Josep Virgili-Llop, and Marcello Romano. «A tip-tilt hardware-in-the-loop air-bearing test bed with physical emulation of the relative orbital dynamics». In: *Adv Astronaut Sci* 168.2019 (2019), pp. 3781–3799 (cit. on p. 20).

[44] Bautista R Fernandez, Leonardo Herrera, Jennifer Hudson, and Marcello Romano. «Development of a tip-tilt air-bearing testbed for physically emulating proximity-flight orbital mechanics». In: *Advances in Space Research* 71.10 (2023), pp. 4332–4339 (cit. on p. 21).

[45] T2 Informatik. *The V-Model – A Process Model for IT Development*. 2025. URL: https://t2informatik.de/en/smartpedia/v-model/#:~:text=IT%20development%20projects-,The%20V%2DModel%20is%20a%20process%20model%20for%20IT%20development,in%201979%20by%20Barry%20W. (cit. on p. 24).

[46] Tamas Vinkó and Dario Izzo. «Global optimisation heuristics and test problems for preliminary spacecraft trajectory design». In: *Advanced Concepts Team, ESATR ACT-TNT-MAD-GOHTPPSTD* (2008) (cit. on p. 24).

[47] Brian Gaudet and Roberto Furfaro. «Robust spacecraft hovering near small bodies in environments with unknown dynamics using reinforcement learning». In: *AIAA/AAS Astrodynamics Specialist Conference*. 2012, p. 5072 (cit. on p. 25).

[48] James Richard Wertz, Wiley J Larson, Douglas Kirkpatrick, and Donna Klungle. *Space mission analysis and design*. Vol. 8. Springer, 1999 (cit. on p. 30).

[49] UiPath Documentation Team. *Hardware Requirements*. Accessed: 2024-12-05. 2023. URL: https://docs.uipath.com/ai-computer-vision/standalone/2023.4/user-guide/hardware-requirements (cit. on p. 30).

[50] Quora User. *What are the hardware requirements for AI development?* Accessed: 2024-12-05. 2024. URL: `https://www.quora.com/What-are-the-hardware-requirements-for-AI-development#:~:text=CPU%2C%20GPU%2C%20RAM%2C%20motherboard,SSDs%20for%20quicker%20data%20access` (cit. on p. 30).

[51] Beebom Staff. *Microsoft Sets 16GB RAM & 40 TOPS of AI Computing Speed as Standard for New 'AI PCs'.* 2024. URL: `https://beebom.com/microsoft-16gb-ram-40-tops-ai-computing-speed-standard-ai-pcs/#:~:text=In%20addition%20to%20all%20this,'&text=Trendforce%20says%20the%20new%20Intel,fall%20short%20of%20Microsoft's%20standards.%E2%80%9D` (cit. on p. 30).

[52] TrendForce. *TrendForce Reports DRAM Prices to Rise by 13–18% in 1Q24 Due to Production Cuts and Supplier Strategy.* Accessed: 2025-03-05. 2024. URL: `https://www.trendforce.com/presscenter/news/20240117-12000.html` (cit. on p. 30).

[53] ASPINA. *Reaction wheel for satellite and CubeSat.* Accessed: 2024-12-05. 2023. URL: `https://eu.aspina-group.com/en/learning-zone/columns/2023022201/` (cit. on p. 32).

[54] Giuseppe Governale, J Rimani, N Viola, and V Fernandez Villace. «A trade-off methodology for micro-launchers». In: *Aerospace Systems* 4.3 (2021), pp. 209–226 (cit. on pp. 35, 36).

[55] Keyan Cao, Yefan Liu, Gongjie Meng, and Qimeng Sun. «An Overview on Edge Computing Research». In: *IEEE Access* 8 (2020), pp. 85714–85728. DOI: `10.1109/ACCESS.2020.2991734` (cit. on p. 38).

[56] NVIDIA. *Jetson Orin: Embedded AI Computing Platform.* 2024. URL: `https://www.nvidia.com/en-us/autonomous-machines/embedded-systems/jetson-orin/` (cit. on p. 38).

[57] NVIDIA Corporation. *Jetson Orin | NVIDIA.* Accessed: 2024-12-05. 2024. URL: `https://www.nvidia.com/en-sg/autonomous-machines/embedded-systems/jetson-orin/` (cit. on p. 40).

[58] New Way Air Bearings. *Design and Application Guide.* 12th. 2021. URL: `https://www.newwayairbearings.com/wp-content/uploads/2021/07/NWAB-Design-and-App-Guide-ver-12-2021.pdf` (cit. on p. 41).

[59] IBS Precision Engineering. *Air Bearing Application Guide.* Accessed: 2024-11-27. n.d. URL: `https://www.ibspe.com/hubfs/Documents/05.4-Technical-Resources/04.-Components/04.-Air-Bearing-Application-Guide.pdf` (cit. on p. 42).

[60] Protoyz. *HPA System 3000PSI with PT Regulator 0.4L Alloy*. `https://www.paintball.shop/hp-air-co2/hp-air-systems/hpa-syst-3000psi-pt-reg-0-4l-alloy-protoyz_21054_21753/` (cit. on p. 44).

[61] Naval Postgraduate School. *Facilities - Advanced Systems and Technology (AST) Research Center*. Accessed: 2024-12-05. 2024. URL: `https://nps.edu/web/ast/facilities` (cit. on p. 44).

[62] Josef Kulke. *Conceptual Design of an Open-Source Hardware Simplified Floating Spacecraft Simulator*. Tech. rep. Monterey, California. Naval Postgraduate School, 2022 (cit. on pp. 44, 47).

[63] Gems Sensors. *E-EH Series Solenoid Valve - EG2035*. Accessed: 2025-03-05. 2025. URL: `https://www.gemssensors.com/search-products/product-details/e-eh-series-solenoid-valve-eg2035` (cit. on p. 45).

[64] Junaidh Shaik Fareedh. *Design, Fabrication and Modelling of Three Axis Floating Satellite Simulator*. 2017 (cit. on p. 51).

[65] Bosch Sensortec. *BNO055 Absolute Orientation Sensor Datasheet*. 2020. URL: `https://www.mouser.it/datasheet/2/783/bst_bno055_ds000-3247202.pdf` (cit. on p. 52).

[66] Indiamart. *40, 50, 60 Feet Low Bed Trailer Transportation Service*. 2025. URL: `https://www.indiamart.com/proddetail/40-50-60-feet-low-bed-trailer-transportation-service-2849895916662.html` (cit. on p. 64).

[67] Goldhofer. *Self-Propelled AddDrive - Heavy Duty Modules*. 2025. URL: `https://www.goldhofer.com/en/heavyduty-modules/self-propelled-addrive` (cit. on p. 65).

[68] GAM Rentals. *Ormig 55/60iE Electric Crane*. 2025. URL: `https://online.gamrentals.com/it/ormig/1887-ormig-55-60ie` (cit. on p. 66).

[69] NMG Italia. *MC-300S Mobile Crane*. 2025. URL: `https://nmgitalia.com/fr/prodotto/mc-300s/` (cit. on p. 66).